Geometrical and transport properties of random packings of spheres and aspherical particles

D. Coelho,[1] J.-F. Thovert,[1] and P. M. Adler[2]
[1]*Laboratoire des Phénomènes de Transport dans les Mélanges (LPTM), SP2MI, Bd 3, Téléport 2, F-86960 Futuroscope, France*
[2]*IPGP, tour 24, 4, Place Jussieu, 75252 Paris Cedex 05, France*
(Received 7 March 1996; revised manuscript received 30 September 1996)

Random packings of grains of arbitrary shape are built with an algorithm that is mostly applied to spheres, ellipsoids, cylinders, and parallelepipeds. A systematic account of the main geometrical properties such as the porosity, the reduced specific area, etc. is given. The conductivity, the permeability, and the dispersion are also systematically determined and they are shown not to depend upon their mode of construction. [S1063-651X(97)13802-8]

PACS number(s): 46.10.+z, 47.11.+j, 81.05.Rm, 47.55.Mh

I. INTRODUCTION

Grain packings have attracted considerable interest for a long time as a model for various types of porous media, such as geological materials like soils, etc. Of course, regular packings have been extensively studied, since their simple geometries make an analytical or semianalytical determination of their properties achievable. However, they do not account for the random character of most natural media. Therefore, we shall not dwell on these models, and focus rather on three-dimensional random packings.

A general numerical algorithm was devised to simulate the random sequential deposition of nonoverlapping grains with arbitrary shapes. The model is three dimensional and accounts for translations and rotations of the particle during their settling. To the best of our knowledge, these features were never found simultaneously in previous simulations. The algorithm was applied to various particle shapes and aspect ratios. The main geometrical and transport properties of the resulting packed beds were systematically determined. Comparisons with prior numerical or experimental data are made whenever possible.

Most of the enormous literature on random packings accumulated during the last decades can be found in recent surveys [1–5]. Brief specific surveys are made in some sections of this paper.

This paper is organized as follows. Section II is devoted to the construction of random packings. Earlier algorithms, which mostly addressed spherical grains, are briefly surveyed. Then, the sequential deposition algorithm is detailed. The search for the rest position of a particle that settles under gravity combines steepest descent and conjugate gradient methods. A weighting coefficient is introduced to favor translational or rotational degrees of freedom.

The geometric properties of the random packings are addressed in Section III. After a short review of the various conceptual and experimental characterization tools, beds of spheres, ellipsoids, cylinders, and parallelepipeds with various aspect ratios are considered and many novel results are given for porosity, specific surface area, orientational ordering, and correlation function. Larger porosities are obtained when either rotation or translation of the settling particles is strongly favored; in between, all the properties are weakly sensitive to the weighting between the translational and rotational degrees of freedom. Whatever the particle shape, minimal porosities are obtained for unit aspect ratios. Oblate ellipsoids are a special case, where a strong ordering in horizontal layers develops. For sphere packings, our results agree with previous data for random loose packings.

Section IV is devoted to the transport properties of the random packings. Conduction, convection, and Taylor dispersion are successively considered. The governing equations and methods of solution are recalled first from earlier works. A unique power law relates the conductivities of all the packed beds to their porosities, regardless of the particle shape, in agreement with the classical Archie's law. Permeabilities are likewise related to porosity only. The data are successfully compared to various models, and a relationship between the Kozeny constant and the grain asphericity index is proposed. Finally, the longitudinal and transverse dispersion coefficients in beds of ellipsoids depend very weakly upon the particle aspect ratio. The numerical results are in very good agreement with numerous experimental data for various granular media.

Some concluding remarks end this paper. Although the geometrical properties of randomly deposited packings depend upon the shape of the constituting grains, their transport properties do not depend upon their mode of construction, when beds with identical porosities and equivalent particle sizes are compared.

II. CONSTRUCTION OF RANDOM PACKINGS

A. Literature survey

The packings investigated in this paper result from the random sequential deposition of nonoverlapping grains as in the pioneering work of Vold [6]. In such a ballistic deposition, the grain trajectories toward their final position are built explicitly, which ensures that a particle can actually reach its position during the genesis of the packing. Similar algorithms were used by many authors such as Visscher and Bolsterli [7] who included a periodicity condition along the horizontal directions, in order to reduce the lateral wall effects (cf. [2] and references therein for a study of these wall effects). These authors generalized also the method to bidisperse sphere packings. Today, such simulations can be done for samples of several millions of spheres [8].

All the aforementioned studies share a few common features. They operate in a continuous space, a feature that improves precision. The particles are dropped one at a time.

The grain interactions (i.e., the nonoverlap condition) are handled analytically; this speeds up the simulations, but limits the applicability to very simple (monodisperse or bidisperse) collections of spheres. The particle does not move anymore after settling. Therefore, the interactions between the particles are limited to the exclusion condition between the currently settling grain and the static configuration of the current bed.

These numerical works have their experimental counterparts. For instance, Bacri *et al.* [9] deposited glass beads in water. Onada and Liniger [10] also deposited glass beads in a viscous fluid, under microgravity conditions by matching the densities of the fluid and solid phases.

Rosato *et al.* [11,12] and Buchalter and Bradley [13,14] tried to take into account the interactions between the settling particles, which may become significant at higher deposition rates, for example, during the settling of concentrated suspensions.

Few attempts have been made to account for the collective rearrangement of grains within the bed by application of Newton's laws of motion. Yen and Chaki [15] accounted for interparticle forces but not for hydrodynamic forces. However, various procedures have been devised to simulate reordering due to shaking or vibrating [5]. A first family of methods increases the packing fraction, by biasing the ballistic deposition procedure [16,7]. Other authors allow rearrangements once a sequentially deposited packing has been built [17,13].

For the sake of completeness, let us mention briefly a few totally different non-ballistic models that were devised by Jodrey and Tory [18], Larson and Higdon [19], and Martys *et al.* [20]. Other authors (e.g., Torquato and Stell [21]) study the properties of random packings whose morphology results from thermodynamical equilibrium hypotheses, without building them. Finally, purely geometric construction procedures have been devised, such as tetrahedral tiling or Voronoi cells, in order to maximize the packing fraction (see, for example, Dodds [22]).

Packings of nonspherical particles have not been computed often in the past and they were only addressed in some recent works by Buchalter and Bradley [13,14] for ellipses and ellipsoids in two and three dimensions.

B. Sequential deposition algorithm

Our random packings result from the successive deposition of grains in a ''gravitational'' field. The grains are introduced at a random location above the bed already in place, and fall until they reach a local minimum of their potential energy. Sometimes, a dynamic language is used, but the reader should not be misled, since the Newton's laws of motion are never solved. During their fall, any displacement and rotation that contribute to lower their barycenter are allowed.

As a general rule, a mobile particle is allowed to slip freely on the bed surface as long as the elevation of the barycenter can be diminished. Moreover, each elementary displacement of a grain is independent of its previous position and orientation increments. However, as described below, an adjustable parameter favors either translation or rotation of the particle, when both motions could lower its elevation. Finally, the interactions are reduced to steric exclusion. A variant of this rule has been devised to simulate short-range attractive forces, which could create permanent links between grains. After contact, a settling grain can be allowed to rotate around the contact point without slip (but the contact may move if the grain rolls on the bed). For instance, for parallelepipedic grains, if a vertex comes in contact with an underlying plane solid surface, the particle would rotate until one of its edges and eventually one of its faces becomes tangent to this surface.

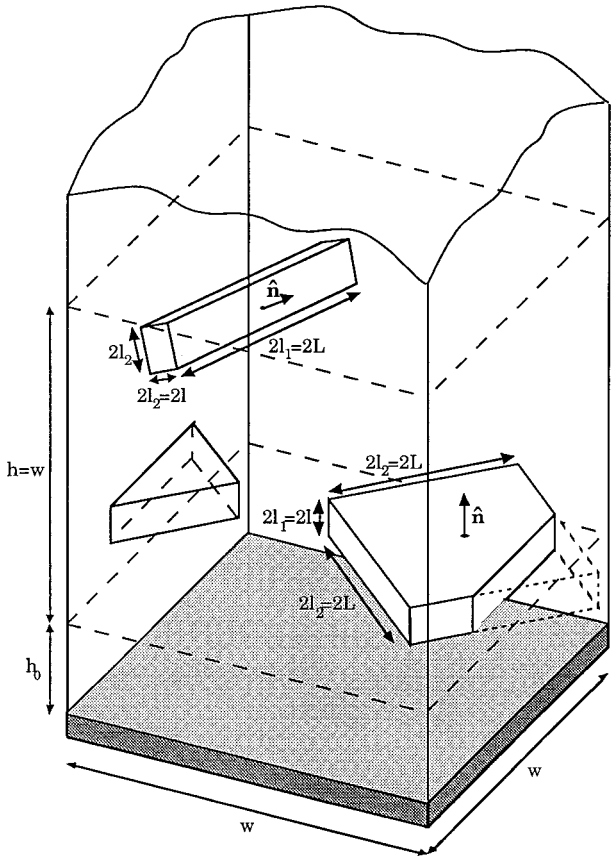

FIG. 1. Schematic diagram of the unit cell with periodic boundary conditions; illustration of some geometrical notations.

An interesting feature of our algorithm is that each particle may have any size and shape, provided that it can be described in a spherical polar coordinates system (r,θ,φ) attached to it by a single valued function $\rho(\theta,\varphi)$. The inner volume of the particle is defined by

$$r \leqslant \rho(\theta,\varphi). \tag{1}$$

Obviously, any convex particle shape can be described by Eq. (1). In this paper, only orthotropic particle shapes have been considered (ellipsoids, circular cylinders, parallelepipeds). Of course, the particle referential is aligned with its principal axes.

The position of a particle is represented by the location $\mathbf{r}={}^t(x,y,z)$ of its barycenter, and by a set ω of three angles that give the orientation of the particle referential, with respect to the coordinate system; the superscript ''t'' denotes the transportation operator. The z axis is oriented upwards. The grains are deposited in a square vertical box, with a flat bottom at $z=0$, and periodicity conditions along the x

and y directions, in order to avoid the well-known hard-wall effects (Fig. 1).

The trajectory of a grain during its settling is built by small elementary steps. Suppose that its current position and orientation are $\mathbf{r}$ and ω. Let $\mathbf{x}={}^t(x,y)$ be its horizontal position. The first step is to determine the number and the positions of the contact points with the bed, below the grain. This is done by scanning the surfaces of the grain and of the neighbor particles that belong to the bed. Two or more simultaneous contact points are a statistically unlikely event, except in the very late stages of the settling, which are specifically addressed, as described below. The most common case is a single contact point, and one has to determine the combined horizontal translation $d\mathbf{x}$ and rotation $d\boldsymbol{\omega}$, which allow the steepest descent dz of the particle barycenter. Formally, we consider the function giving the (locally) lowest elevation and orientation $z(\mathbf{x},\omega)$, and evaluate its gradient $\boldsymbol{\nabla}_z$. This is done analytically, since the normal and tangential vectors to the contacting surfaces can be derived from the definitions (1) of the particle shape. Note that this quantity is purely local and that it takes into account the detected contacts, but not the possible presence of the other close solid walls. Moreover, it ignores the curvatures of the grain and of the bed surfaces.

The direction that yields the steepest descent is the couple $(\delta\mathbf{x},\delta\boldsymbol{\omega})$, which maximizes the absolute value

$$\delta z=|\boldsymbol{\nabla}_{\mathbf{x}}z\cdot\delta\mathbf{x}+\boldsymbol{\nabla}_{\omega}z\cdot\delta\boldsymbol{\omega}|. \tag{2a}$$

At this stage, the amplitude of the displacement is unknown and it is arbitrarily set to 1; hence,

$$\delta\mathbf{x}^2+\hat{R}^2\,\delta\boldsymbol{\omega}^2=1. \tag{2b}$$

Note that the angular increment $\delta\omega$ is weighted by a length $\hat{R}$, which is kept constant for a given particle, and is generally equal to the radius of the sphere with the same volume. Note, however, that $\hat{R}$ can be chosen to tune the preferential motions of a particle. Small values of $\hat{R}$ favor translation $\delta\mathbf{x}$ in Eq. (2a) since the particle will lower its position mostly by translations. The reverse holds for large values of $\hat{R}$.

Once the direction $(\delta\mathbf{x},\delta\boldsymbol{\omega})$ of the displacement has been deduced from Eq. (2), it is applied to the particle with an amplitude A, small with respect to the particle size (say $A\leqslant\hat{R}/5$). The actual lowest possible position z' of the grain at $(\mathbf{x}+A\,\delta\mathbf{x},\boldsymbol{\omega}+A\,\delta\boldsymbol{\omega})$ is evaluated. Note that this is done by using the same algorithm as for the detection of the contact points, which scans the surfaces of the grain and of the neighbor particles that belong to the bed. Finally, the steric condition is satisfied within a tolerance (e.g., $\leqslant\hat{R}/1000$).

This steepest descent method is recursively applied as long as a significant downward progress is possible. However, it happens very often that the settling grain enters a ''valley'' between two opposite solid surfaces. The main slopes of these surfaces can be directed in almost opposite directions, and the grain starts bouncing from one side to another, with little vertical progress because the search algorithm is unable to find the major downstream direction of the valley. If at some stage, two contacts are simultaneously found on two opposite faces within a tolerance Δr, a new direction of progression can be enforced. The two tangential planes to the contact points form a dihedron, and the optimization in Eq. (2a) is performed by imposing additional constraints to Eq. (2b), thereby reducing the degrees of freedom. The grain is forced to move along the longitudinal axis of the valley, and as a result, it escapes faster from the trap.

Very often, double contacts cannot be detected before progression becomes exceedingly slow. When this happens, the steepest descent method is replaced by a conjugate gradient algorithm. In this latter algorithm, all the directions of displacement are conjugated (essentially normal) with the directions of the previous steps. This is less efficient than the steepest descent algorithm when the grain slides freely along a long inclined regular surface and for this reason the latter is generally preferred; but in the kind of traps mentioned above, the right direction is almost immediately found. However, when the grain goes back to a larger region, the conjugate gradient algorithm becomes again less efficient than the steepest descent method and it is replaced by it.

Let us mention the specific treatment of triple contacts. This situation is very uncommon if the grain has not reached its final rest position. Then, the analytical evaluation of $\boldsymbol{\nabla}_{\omega}z$ becomes untractable because of the very complex limitations of the rotational degrees of freedom. The optimization (2a) is restricted only to translational displacements ($\delta\boldsymbol{\omega}=\mathbf{0}$).

The settling of the grain ends up when its barycenter cannot be lowered by more than a quantity Δr neither by the steepest descent, nor by the conjugate gradient method. In this final situation, it rests on three simultaneous contacts with a probability of about 0.8 for ellipsoids, and of about 0.5 for sharp edged particles such as cylinders or parallelepipeds.

Various complications may occur, that are fully described by Coelho [23]. For the sake of clarity, the overall deposition algorithm is sketched in Fig. 2.

C. Parameters of the numerical simulations

1. Definition of the grains

Only packings of identical particles with three symmetry planes are investigated in this paper. Ellipsoidal, cylindrical, and parallelepipedic grains were considered. They are defined by their semiaxes $(l_1,l_2,l_3=l_2)$, two of them being equal. For convenience, the semiminor and semimajor axes are also defined by

$$l=\min(l_1,l_2),\quad L=\max(l_1,l_2). \tag{3}$$

Oblate (prolate) particles correspond to $l_1=l$ $(l_1=L)$. The particle orientation is characterized by the axial unit vector $\hat{\mathbf{n}}$ along l_1, which is oriented upwards (Fig. 1).

The following quantities are introduced for later use. The equivalent radius R_v is the radius of the sphere with the same volume. For example, for an ellipsoidal particle, $R_v=l_1^{1/3}l_2^{2/3}$. S_v is the surface area of the sphere of radius R_v. Finally, the sphericity index Ψ is equal to S_v/S, where S is the grain surface area.

2. Overall dimensions of the samples

The packings are built by sequentially depositing a total number of N_u particles in a ''box'' with a square $w\times w$ horizontal cross section (Fig. 1) and a flat hard bottom. In

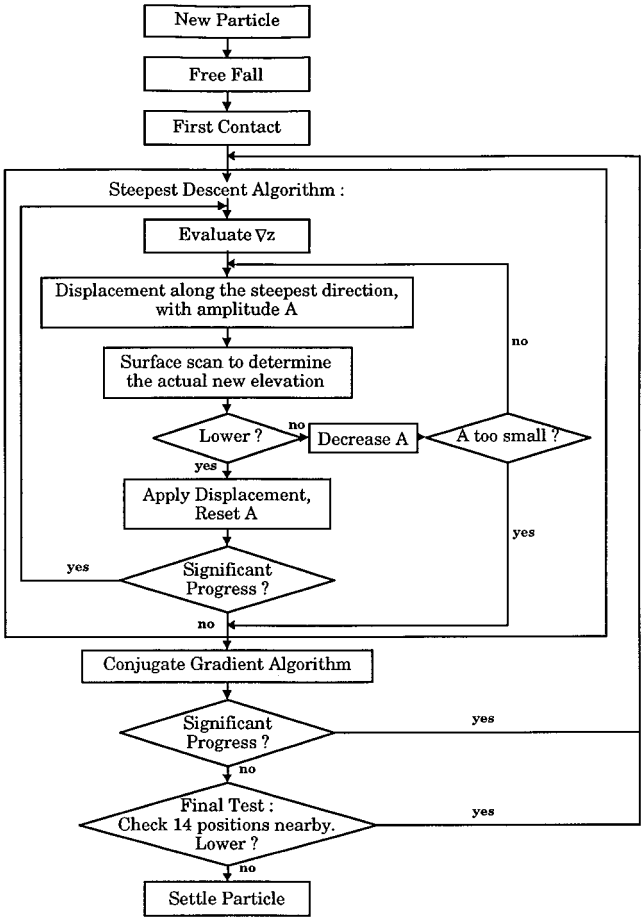

FIG. 2. Sketch of the overall deposition algorithm.

order to minimize size effects, periodicity conditions are applied along the two horizontal directions and all subsequent measurements and calculations are performed in a cubic subsample of volume w^3, which starts at a height h_0 over the bottom of the packing.

The sample size w was always taken much larger than the particle major axis, with $5 \leqslant w/L \leqslant 20$, except for very elongated shapes with $L/l = 10$ where $3 \leqslant w/L \leqslant 5$. The rejected layer thickness h_0 is always at least equal to $w/2$. Porosity measurements within layers at increasing elevations show that the disturbances induced by the flat bottom do not extend beyond this range.

3. Parameters of the search algorithm

Four parameters have been introduced in the sequential deposition algorithm described above. One of them, the weighting length $\hat{R}$ in Eq. (2a) has been varied from half the minor axis up to twice the major axis of the particles, and it does influence the resulting packings, as discussed in Sec. IV. Since the characteristics of the packings were found weakly sensitive to $\hat{R}$ if $L/2 \leqslant \hat{R} \leqslant L$ (and the minimal porosity is obtained in this range), most simulations were performed in this condition. However, it should be emphasized that in Sec. IV, the transport properties of the packings can be related to their geometrical characteristics regardless of this construction parameter.

The three other parameters involved in the deposition algorithm, namely A, Δr, and $\Delta\omega$, control the step sizes and the accuracy of the search for the equilibrium positions, but they do not influence the final result, provided that they are small enough.

4. Statistical fluctuations and sensitivity to the numerical parameters

Since the building of the packed beds is a stochastic process, their properties are expected to show some statistical fluctuations. It is useful to quantify this dispersion, in order to set the values of A, Δr, and $\Delta\omega$ accordingly. Since very fine requirements are very costly in terms of computational time, it is pointless to try to achieve an accuracy much smaller than the statistical fluctuations. It may be useful to anticipate on the discussion of Sec. III.

Systematic studies on the statistical fluctuations were performed. For instance, the standard deviation σ_ϵ of the porosity for beds of spheres of radius R is 0.0048 when $w = 10R$ while the average porosity is 0.4121. Larger fluctuations were expected for aspherical particles. The porosities of three realizations of packings of oblate ellipsoids with $l_1/l_2 = 5$, $w/L = 7.02$, $A = R_v/5$, $\Delta z = R_v/50$, and $\Delta\omega = 0.87°$ ranged between 0.414 and 0.449. This order of magnitude of the fluctuations is valid for all the simulations reported in this paper, except for very flat oblate ellipsoids with $l_1/l_2 = 0.1$. In the latter case, the grains tend to settle with their largest section horizontal. This would yield a well-organized bed with a porosity comparable to that for less aspherical grains. However, a few grains may get clamped in inclined positions, with their edge stuck between two particles. This rare event has dramatic consequences, since it disturbs the arrangement of the surrounding particles over distances of order L. This is illustrated in Fig. 3, for ellipsoids with $l_1/l_2 = 0.1$, and $w/L = 7.43$. These two beds have porosities 0.395 and 0.569. Such effects are less critical for prolate particles, since the disturbances induced by one grain are weaker, and are smoothened for moderately oblate particles, because larger ratios w/L could be used.

In view of these statistical fluctuations, the porosity cannot be used to test the influence of the search parameters A, Δr, and $\Delta\omega$. Instead, the overlap between the solid grains was considered. The complete study is reported by Coelho [23]; it may be summarized by saying that in the worst cases, the average overlap thickness is smaller than $R_v/100$.

5. Computations

For each particle shape, three main series of simulations were run, which cover the whole range of aspect ratios l_1/l_2; for the sake of completeness, their parameters are summarized in Table I.

Except in the special case of spheres, the numerical computations for the deposition of a single grain require about 20 s on an IBM RS6000-560 workstation. The total time consumed to build the samples used in this study amounts to about 500 h, including the burden to build the rejected lower layer, and the upper layer of comparable height.

III. GEOMETRIC PROPERTIES OF RANDOM PACKINGS

A. Geometrical description of random packings

The purpose of this subsection is to summarize the various characteristic geometrical parameters that are defined in

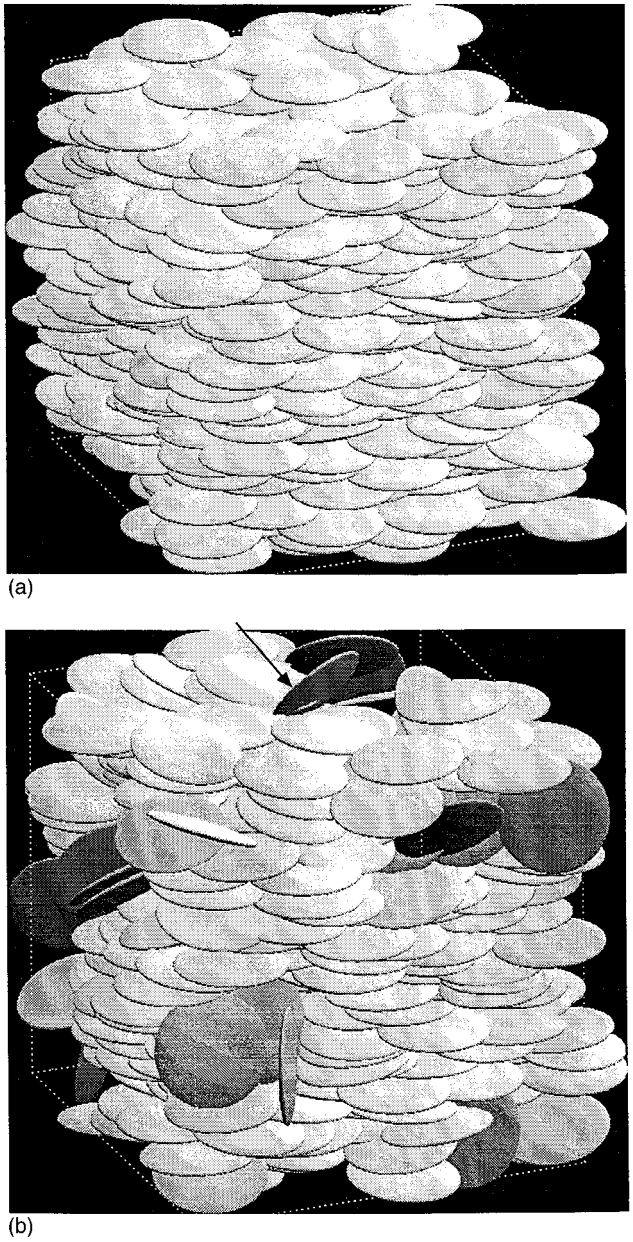

FIG. 3. Two packings of oblate ellipsoids with $l_1/l_2=0.1$. The porosity is 0.395 (a) and 0.569 (b). The overlap of two grains is indicated by the arrow in (b).

[24,25,3]. In addition to the determination of the constituting grains, which is of no interest for numerical packings, the quantities to be characterized fall into several categories, namely the global parameters, the pore space morphology, and ordering. The global parameters include the porosity ϵ or the solid fraction $\phi=1-\epsilon$, and the specific surface area $\mathcal{S}$. A variety of mathematical tools has been introduced to characterize the morphology of the pore space, such as various types of one- or two-dimensional size distributions, mean free path, etc. [24,3]. Finally, various parameters have been defined to describe the short or long range ordering of the grains within the bed, such as the coordination number Z (average number of contacting grains), the radial distribution function g, and the orientational or positional ordering indices.

TABLE I. Search algorithm parameters and typical sample contents (number of particles N_u).

	Series			
	1	2	3	Tests
$\hat{R}$	(0.2–0.5) L	(0.1–0.3) L	(0.5–1) L	(0.5–1) L
A	$R_v/5$	$R_v/5$	$R_v/5$	$R_v/20$
Δr	1/100	1/100	$R_v/50$	$R_v/200$
$\Delta\omega$	1/2°	1/2°	5/6°	1/2°
N_u	50–500	150–300	300–600	300–600

Access to these parameters is more or less easy depending on whether one deals with a real or a synthetic sample. Among commonly used experimental methods, one can cite image analysis, gas sorption, nuclear magnetic resonance [3], mercury intrusion porosimetry [25], and finally, diffraction patterns from small angle scattering (SAS) [3].

The situation seems easier when the packed bed is described numerically, for example, by all the grain positions and orientations. Volume fractions, specific surface area, radial distribution functions, and orientational correlations are indeed readily available. Diffraction patterns equivalent to SAS measurements can also be obtained by Fourier transform [13,14]. However, some quantities are still tricky to determine. The coordination number Z, which is mostly used in theoretical approaches [26], can easily be underestimated by failing to detect contacts. The determination of the connectivity and pore size distribution of the pore space is also a difficult task as can be seen in [27–30].

In this paper, in addition to porosity and specific surface area, ordering parameters are investigated, such as the radial distribution function, the positional ordering via the two point phase correlation function, and the orientational ordering via angular correlations.

B. Porosity

The simplest characteristic quantity of the packing geometry is its porosity, or void volume fraction ϵ. The influence of the construction parameter $\hat{R}$ was investigated first. Packings of aspherical ellipsoids (with $l_1/l_2=1/5$, $1/\sqrt{10}$ and $\sqrt{10}$), cylinders (with $l_1/l_2=5$), and parallelepipeds (with $l_1/l_2=1/\sqrt{10}$ and $\sqrt{10}$) were built with various weighting lengths $\hat{R}$; the other parameters are identical to the ones used in series 3 in Table I. The resulting porosities are plotted in Fig. 4(a) against the ratio $\hat{R}/L$. Larger porosities are obtained for small and large values of this ratio. This can be explained by the fact that for very small (large) $\hat{R}$, the deposition algorithm first tries to lower the grain elevation by shifting its horizontal position (by rotating it) without rotation (horizontal shift), whereas for moderate $\hat{R}$ all the grain degrees of freedom are simultaneously considered. It is remarkable that for all particle shapes and types (prolate or oblate), the minimal porosity is always obtained for $\hat{R}$ ranging from $L/2$ to L. Therefore, it is expected that the packing properties are weakly sensitive to $\hat{R}$, if it is set in this range.

Consider now the complete data in Fig. 5. The porosities of all the packed bed samples are plotted against the ratio l_1/l_2. According to Fig. 4 and the range of $\hat{R}$ in Table I, porosities of series 2 are expected to be larger than for series

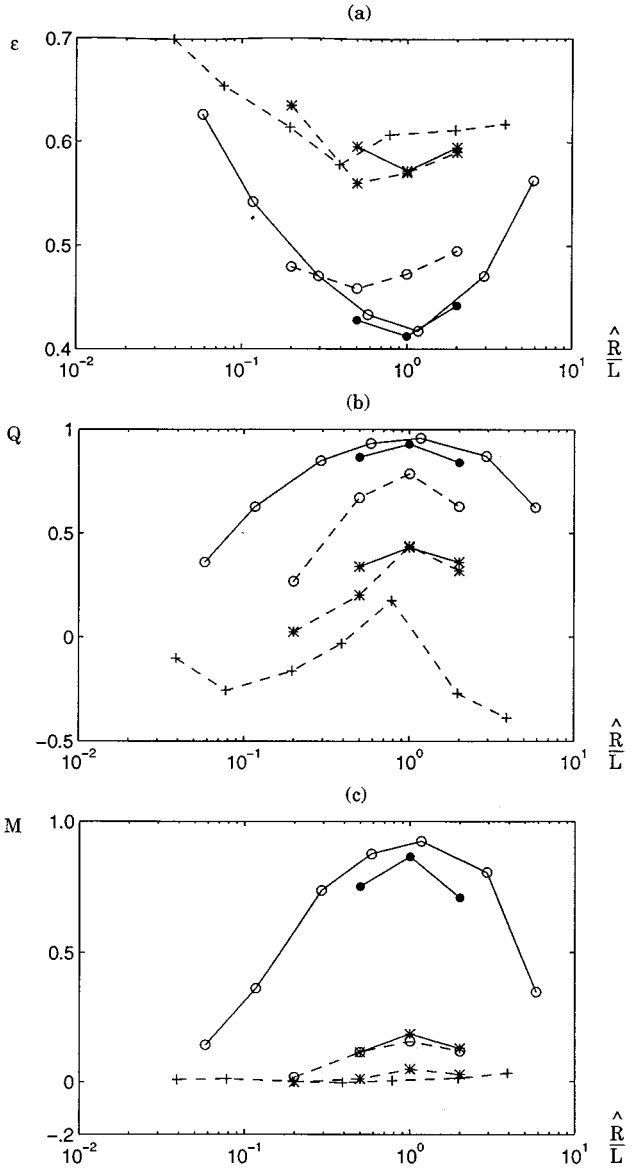

FIG. 4. The porosity ϵ (a), angular correlations Q (b), and M (c) vs the ratio $\hat{R}/L$ for beds of oblate (—) or prolate (---) particles. Data are for ellipsoids with $L/l=5$ (○) or $\sqrt{10}$ (●), cylinders with $L/l=5$ (+) and parallelepipeds with $L/l=\sqrt{10}$ (∗).

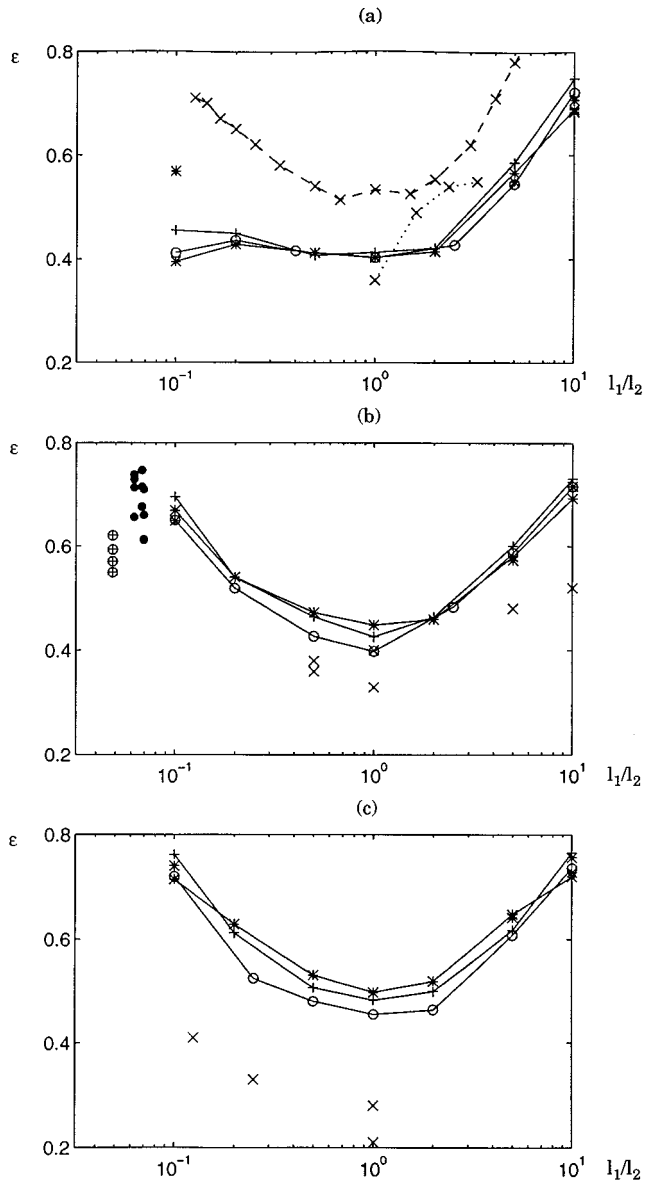

FIG. 5. The porosity ϵ of packings of ellipsoids (a), cylinders (b), and parallelepipeds (c) vs the aspect ratio l_1/l_2. The numerical data (solid lines) are for series 1 (○), 2 (+), and 3 (∗). The broken line in (a) corresponds to the data of [14] and the dotted line to those of [34]. The crosses in (b) and (c) are data from [2]. In (b), the data of [33] for mica particles are denoted by ● and those for mylar disks by ⊕.

1, which are themselves larger than those of series 3. This is actually observed only for the most extreme size ratios. For $L/1\leqslant 5$, the statistical fluctuations and maybe the slight differences in the search parameters A, Δr, and $\Delta\omega$ prevent an obvious display of this ordering. As a matter of fact, series 3, with a larger R but looser parameters (Δr,$\Delta\omega$), often yields the largest porosities for sharp-edged particles.

The curves for the various particle shapes share a few common features. They all show a minimum for the unit aspect ratio. For prolate grains, the porosity increases with l_1/l_2. For very elongated particles, all the curves seem to converge toward a common value. This is because the grain packings become bundles of needlelike particles, whose cross sections have little influence on their relative arrangement. However, for oblate grains, different behaviors are observed for ellipsoids and sharp-edge particles (cylinders or parallelepipeds). The porosity of cylinders and parallepipeds packings increases with l_1/l_2, whereas it remains almost constant for ellipsoids. This will be discussed below in relation with the orientational ordering within the bed.

Finally, let us compare these data with the available numerical and experimental results of the literature. It is natural to start with random packings of monodisperse spheres. Experimental data are somewhat scattered because of the various packing construction processes and porosity ranges from 0.336 up to 0.445 [31,9,10,32,1]. The porosity of real packings decreases with the apparent gravity, and with subsequent shaking or vibrating procedures. It is generally agreed that 0.3644 ± 0.0004 is the lowest porosity achievable without any significant increase of short-range order [1]. Our

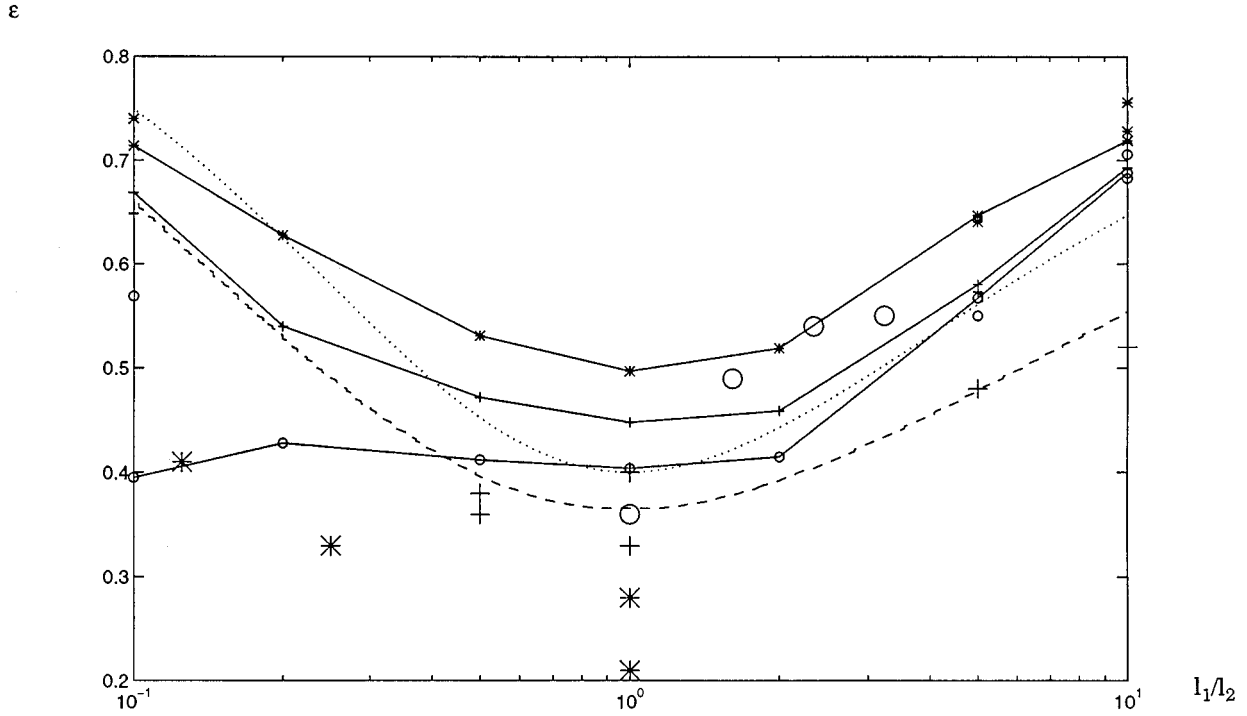

FIG. 6. The porosity ϵ of packed beds vs the aspect ratio l_1/l_2. The numerical data (solid lines) are for ellipsoids (○), cylinders (+), and parallelepipeds (∗). The broken line is model (4) and the dotted line is model (5). The large symbols are the data of [34] for ellipsoids (○) and of [2] for cylinders (+) and for parallelepipeds (∗).

simulations, which yield $\epsilon=0.402$, are in the middle of the range 0.40 ± 0.02 quoted by Berryman [1] for the so-called random loose packings; they also agree with the recent simulations of Jullien and Meakin [8] and Barker [5], who obtained $\epsilon=0.4185$.

Numerical and experimental data for aspherical grain packings are much scarcer and our results can be considered as the first systematic study of such particles. A short list of porosities for cylinder and parallelepiped packings is quoted from various sources by German ([2], Table 5.1). They are compared with our results in Fig. 5. Although they show comparable variations with the aspect ratio l_1/l_2, they are significantly lower than the numerical data (by about 0.10 for cylinders and 0.20 for parallelepipeds). The data of Kim *et al.* [33] for beds of mica particles are consistent with our results as shown in Fig. 5(b), while the values for mylar disks are somewhat lower. Submicronic silica-hematite prolate ellipsoids were prepared and packed by a filtration process by Thies-Weesie *et al.* [34]. The porosity was measured during permeation, since the packed beds expand in the rest state due to surface charge repulsive forces. Their data, plotted in Fig. 5(a), are somewhat larger than ours, perhaps because of these repulsive forces, and because the beds are not formed by a sequential sedimentation process, but rather by a fast convection driven compaction. For this latter reason, these packings could be better described by the numerical simulations of Buchalter and Bradley [14], whose model accounts for the particle interactions during the packing construction.

Finally, let us mention two purely empirical correlations used to predict the void fraction in random packings of aspherical grains which relate the sphericity index Ψ to the solid fraction ϕ:

$$\Psi = 0.079 + 0.831\phi + 1.53\phi^3, \tag{4}$$

$$\phi = \frac{q}{(36\pi)^{1/3}}\,\Psi. \tag{5}$$

These models due to Warren and German [35] and Thies-Weesie *et al.* [34], respectively, are compared in Fig. 6 with our data of series 3 and the various experimental data mentioned above. The constant q was set equal to 2.9 in order to match our results for spheres ($\Psi=1$). Model (4) describes fairly well the experimental data for cylindrical grains packings, and model (5) agrees with our data for prolate ellipsoid packings, but these correlations based on the sphericity index are clearly not universal.

C. Specific surface area

The second quantity that is widely used to characterize porous media, and thus grain packings, is the specific surface area $\mathcal{S}$, defined as the total solid surface area per unit volume, multiplied by the length scale R_v. For packings of identical grains $\mathcal{S}$ is given by

$$\mathcal{S} = \frac{3\phi}{\Psi}. \tag{6}$$

The hydraulic radius m is defined as the ratio of the total pore volume to its surface area. For packings of identical particles, one has

$$\frac{m}{R_v} = \frac{\epsilon}{\mathcal{S}} = \frac{\epsilon\Psi}{3\phi}. \tag{7}$$

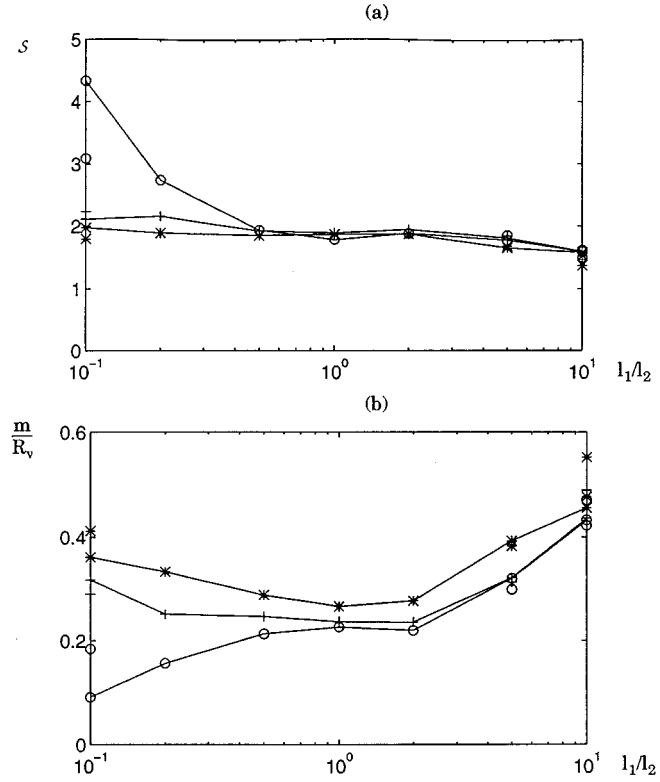

FIG. 7. The reduced specific area $\mathcal{S}$ (a) and hydraulic radius m/R_v (b) vs the aspect ratio l_1/l_2 for packed beds of ellipsoids (○), cylinders (+), and parallelepipeds (∗).

The specific surface area $\mathcal{S}$ is plotted in Fig. 7(a) as a function of the aspect ratio l_1/l_2 for the various particle shapes. Only data for series 3 are displayed since identical trends are observed with series 1 and 2. All the prolate particles follow the same behavior, with a slight decrease of $\mathcal{S}$ as the particles become more slender. For oblate cylinders and parallelepipeds, $\mathcal{S}$ increases slightly when the grains become thinner. However, a different trend is observed for oblate ellipsoids with a sharp increase of the surface area. This results from the smooth ordering of the particles. As already pointed out, the porosity remains roughly constant whatever the aspect ratio l_1/l_2, whereas the asphericity index Ψ drops for oblate spheroids. Hence, their ratio $\mathcal{S}$ in Eq. (6) increases.

The hydraulic radius m is plotted in Fig. 7(b) as a function of the aspect ratio for the same configurations as $\mathcal{S}$ above. As a general rule, for a given value of l_1/l_2, the ellipsoidal and parallelepipedic grains yield the smaller and larger ratios m/R_v, respectively. The hydraulic radius increases when the particles become more aspherical, except again for oblate ellipsoids. In this case; both ϵ and ϕ in Eq. (7) remain roughly constant, while Ψ drops down to 0.418 for $l_1/l_2=0.1$.

D. Orientational grain ordering

The orientational grain ordering is characterized by two parameters Q and M. The first one correlates the particle orientations with the vertical axis

$$Q=\begin{cases} \frac{3}{4}\{\langle\cos[2\cos^{-1}(\hat{\mathbf{n}}\cdot\hat{\mathbf{g}})]\rangle+\frac{1}{3}\} & (l_1<l_2) \\ -\frac{3}{2}\{\langle\cos[2\cos^{-1}(\hat{\mathbf{n}}\cdot\hat{\mathbf{g}})]\rangle+\frac{1}{3}\} & (l_1>l_2) \end{cases}, \tag{8}$$

where $\hat{\mathbf{g}}$ is the unit vertical vector and the angular brackets denote the average over all the particles. The constants are set so that $Q=0$ if the axial vector $\hat{\mathbf{n}}$ (see Sec. II C 1) is uniformly distributed over the unit sphere, and $Q=1$ if all the particles lay flat (i.e., with $\hat{\mathbf{n}}$ parallel to $\hat{\mathbf{g}}$ for oblate particles and $\hat{\mathbf{n}}$ perpendicular to $\hat{\mathbf{g}}$ for prolate ones). The second one is a pair correlation of the particle orientations

$$M=\tfrac{3}{4}\{\langle\langle\cos[2\cos^{-1}(\hat{\mathbf{n}}_i\cdot\hat{\mathbf{n}}_j)]\rangle\rangle+\tfrac{1}{3}\}, \tag{9}$$

where the double brackets denote the average over all particle pairs. Again, $M=0$ if the axial vectors are uncorrelated, and $M=1$ if all the particles are aligned.

The influence of the construction parameter $\hat{R}$ upon Q and M was also studied and the results are plotted in Figs. 4(b) and 4(c). Both parameters Q and M are consistently found maximal for $\hat{R}$ equal to the particle semimajor axis L, even in cases where only weak angular correlations are observed. Underweighting or overweighting of the grain rotations during their fall both tends to lessen the global ordering within the bed.

The complete data for Q and M are plotted versus the aspect ratio l_1/l_2 in Figs. 8 and 9, respectively. Oblate and prolate particles clearly exhibit very different behaviors. The angular correlation Q is almost unity for very flat ellipsoids. This explains why the porosity of oblate ellipsoids is almost insensitive to the aspect ratio. If the grains lie almost flat, the bed is actually equivalent to a bed of spheres, dilated along the horizontal directions by a ratio L/l, which does not affect its void fraction.

Due to their sharp edges, flat cylinders and parallelepipeds are not deposited as smoothly as flat ellipsoids. However, significant correlations are still observed, with $Q\sim0.6$ and 0.5 for cylinders and parallelepipeds at $l_1/l_2=0.1$, respectively. The singular nature of line and point contacts also induces stronger fluctuations and a stronger sensitivity to the simulation parameters. For identical aspect ratios, the highest Q is always associated with the lowest ϵ.

For oblate particles, the pair angular correlation M behaves very much like Q, though it is slightly smaller. This means that the particle axes are evenly distributed around the vertical direction.

For a unit aspect ratio, both Q and M almost vanish, as could be expected. Note that these parameters are undefined for spheres.

The observations for prolate particles are totally different. Though it seems that Q decreases with l_1/l_2 for ellipsoids, no clear trend can be pointed out for cylinders or parallelepipeds. Q undergoes very large statistical fluctuations and is very sensitive to the search parameters, with the hierarchy between series 1, 2, and 3 expected from Fig. 4(b) and Table I. Unlike for oblate particles, large differences in Q have no significant influence on porosity, as shown in Fig. 8. However, the pair correlation M is always very close to zero, because of the absence of interparticle arrangements.

The numerical simulations of Buchalter and Bradley [14] for three-dimensional random packings ellipsoids are plotted in Fig. 8. For prolate particles, they are found between series 1 and 2, where the angular displacements are slightly weighted in Eq. (2a). For oblate particles, they fall way below all our simulations. This probably occurs because in

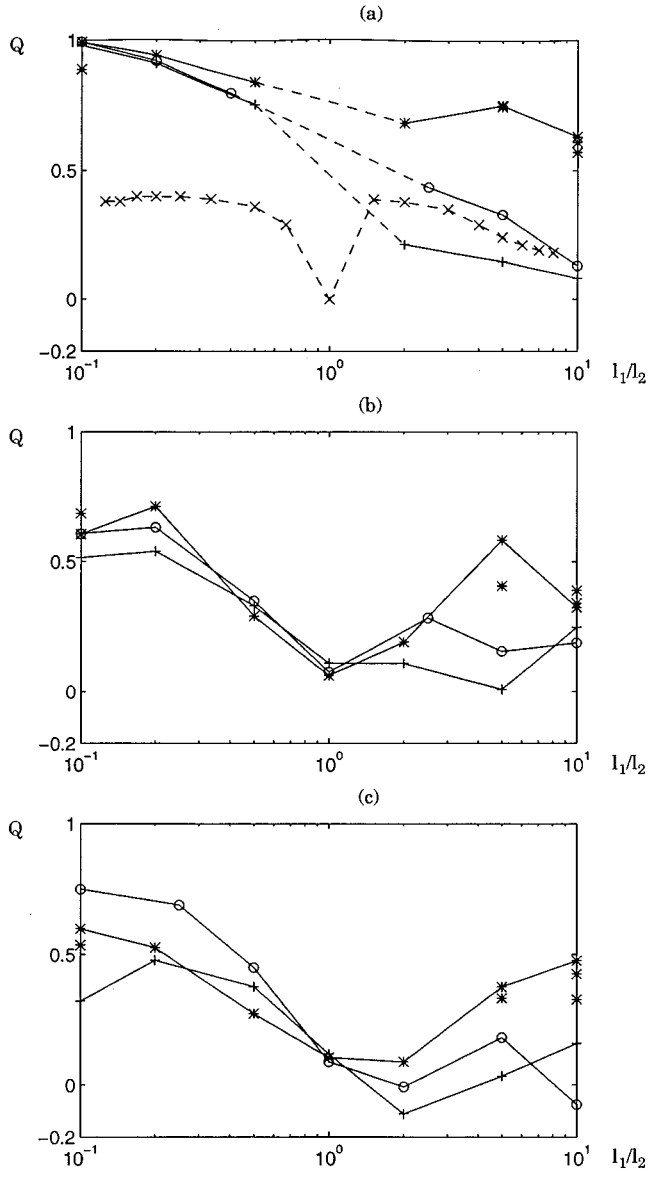

FIG. 8. The orientational ordering correlation Q in beds of ellipsoids (a), cylinders (b), and parallelepipeds (c) vs the aspect ratio l_1/l_2. Same conventions as in Fig. 8.

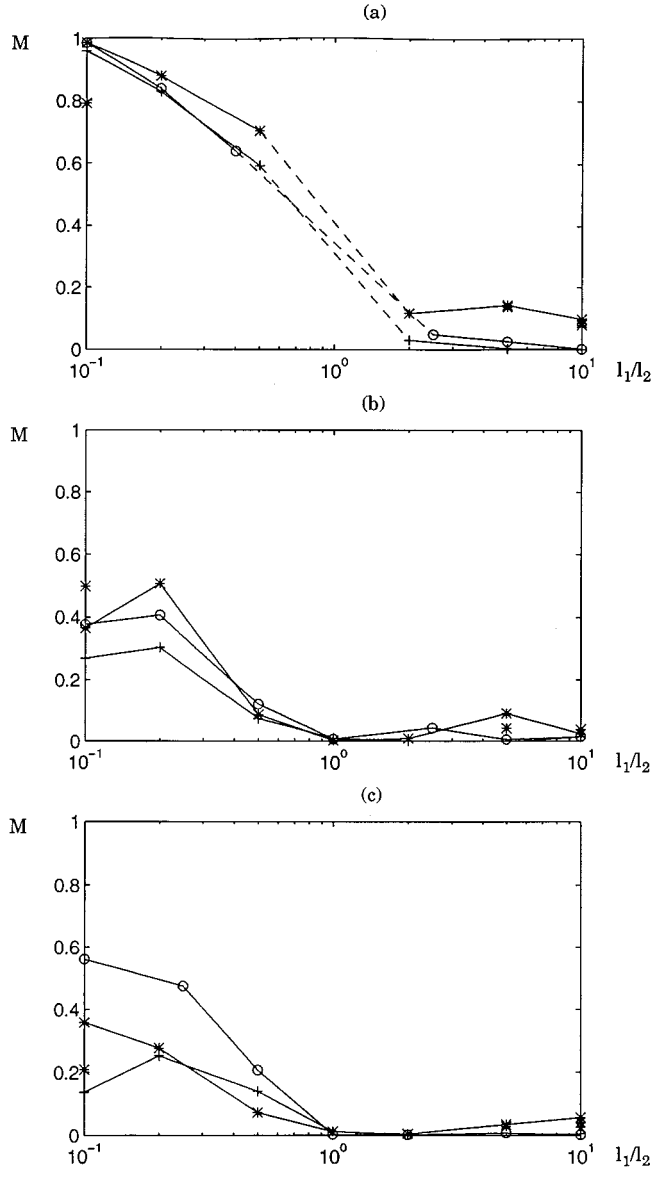

FIG. 9. The orientational ordering correlation M in beds of ellipsoids (a), cylinders (b), and parallelepipeds (c) vs the aspect ratio l_1/l_2. Same conventions as in Fig. 8.

their Monte Carlo simulations, all the grains simultaneously settle in a concentrated suspension; thus, their rotational degrees of freedom are hindered, especially for oblate particles. It may also result from too large angular steps in the random displacements. This step is not reported in Buchalter and Bradley [14], but was taken equal to 6° in a former similar work for two-dimensional ellipsoidal grains [13].

E. Phase correlation function

Let Z denote the phase function describing the void-solid distribution within the bed:

$$Z(\mathbf{r})=\begin{cases}1 & \text{if } \mathbf{r}\in \text{void space}\\ 0 & \text{otherwise.}\end{cases} \tag{10}$$

The statistical average of Z (denoted by an overbar) is the porosity ϵ

$$\epsilon=\overline{Z}. \tag{11}$$

The two-point correlation function R is defined as

$$R(\mathbf{r})=\frac{\overline{[Z(\mathbf{x})-\epsilon][Z(\mathbf{x}+\mathbf{r})-\epsilon]}}{\overline{[Z(\mathbf{x})-\epsilon]^2}}. \tag{12}$$

It measures the probability of finding the two end points of a segment of length $\mathbf{r}$ within the same phase, void or solid. When the medium is macroscopically homogeneous, the statistical averages can be replaced by spatial averages. If the material is isotropic, R is a function of the distance $r=\|\mathbf{r}\|$ only. Grain packings resulting from a deposition process under gravity are not expected to be isotropic, but all the horizontal directions play equivalent roles. Therefore, in the fol-

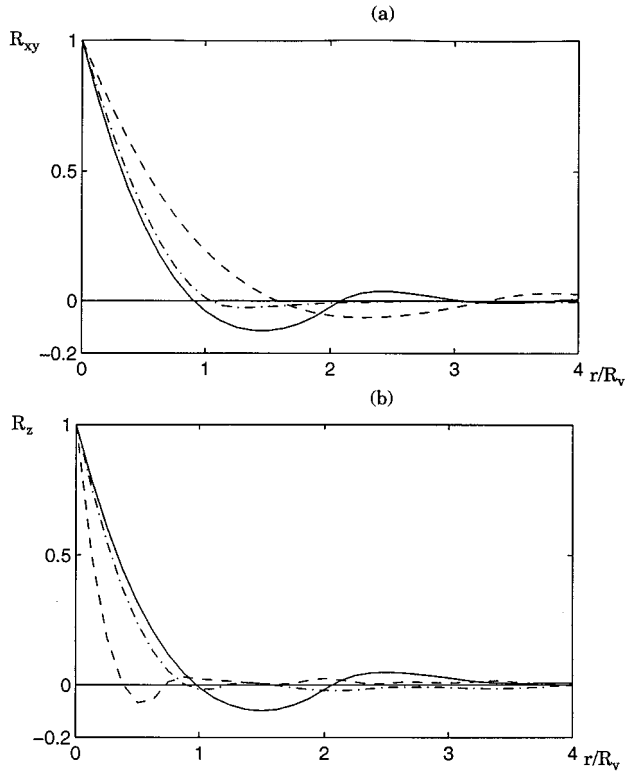

FIG. 10. The correlations R_{xy} (a) and R_z (b) in beds of ellipsoids vs the reduced distance r/R_v. The aspect ratio l_1/l_2 is 0.2 (---), 1 (—), and 5 (-·-·-).

lowing $R_{xy}(r)$ and $R_z(r)$ will denote the correlations evaluated with $\mathbf{r}$ in Eq. (12) set parallel and normal to the horizontal plane, respectively.

Note that the function R includes information relative to the specific surface area. It may be shown that $\mathcal{S}$ is related to the initial slope of R by

$$\mathcal{S}=-4\epsilon(1-\epsilon)R_v \left.\frac{dR}{dr}\right|_{r=0}. \tag{13}$$

This relation holds even for anisotropic media provided that dR/dr is averaged over all the unit sphere [36]. For packings of identical grains, Eqs. (6) and (7) can be used to relate the initial slope of R directly to the asphericity index Ψ or to the hydraulic radius m:

$$\left.\frac{dR}{dr}\right|_{r=0}=-\frac{3}{4\epsilon\Psi R_v}=-\frac{1}{4\phi m}. \tag{14}$$

The correlations R_{xy} and R_z have been evaluated on all the samples considered in this paper. For the sake of clarity and brevity, only data relative to series 3 and ellipsoids, for aspect ratios 1/5, 1, and 5, are reported in Fig. 10. The correlations along the two horizontal directions x and y were always found identical within the statistical fluctuations.

Consider first the correlations along an horizontal direction R_{xy}. The distances are scaled by the equivalent radius of the particles R_v. A first zero crossing at a distance $r\approx 0.90R_v$ is followed by an anticorrelation, up to $r\approx 2R_v$. No significant correlation remains beyond $r\approx 3R_v$ ($|R|<10^{-2}$). For oblate particles with $l_1/l_2=0.2$, the correlation curves look like a stretched version of the former. This is easily understood for ellipsoids, since they are mostly arranged with their largest section horizontal ($Q\geqslant 0.9$). The packed bed is approximately equivalent to a packing of spheres of radius L with the vertical axis scaled by a factor L/l. Thus, the correlation R_{xy} is expected to be the same as for a packing of spheres with radius L. Accordingly, the first zero crossing of R_{xy} for flat ellipsoids is found at $r\approx 0.92L$.

Correlations for packings of prolate particles follow a totally different trend. The first part of the curves, up to the first zero crossing, is very close to the curve for unit aspect ratio. Beyond this point, the correlations vanish almost totally.

Consider now the correlations R_z along the vertical direction. Note first that for sphere packings, R_z is almost identical to R_{xy}. Hence, the material is fairly isotropic, although it results from a construction process that is anisotropic in character. This holds in a lesser respect for the other particle shapes; the initial decrease of the curves for R_{xy} and R_z are identical, but the first zero crossing of R_z is slightly shifted further away from the origin. For the same reason as above, R_z for oblate ellipsoids can be deduced from R_z for spheres with radius l. The first zero crossing is about $1.1l$. Finally, R_z for packings of oblate particles starts with the same initial slope as for unit aspect ratio, but drops to zero more rapidly and vanishes beyond this point.

For spherical grains, positional correlations are very often characterized by the so-called radial distribution function $g(r)$, which measures the probability of finding the center of a grain at a given distance from a reference one [37–39]:

$$g(r)=\frac{1}{4\pi r^2}\frac{d\mathcal{N}(r)}{dr}, \tag{15}$$

where $\mathcal{N}(r)$ is the average number of grain centers within a sphere with radius r around the center of a reference particle. Since $\mathcal{N}(r)$ may have stepwise variations, the derivative in Eq. (15) is not always defined in the usual sense. Besides, these discontinuities are a direct measurement of the bed coordination number.

Results for ellipsoids are given in Fig. 11. In Fig. 11(a) the center-to-center distance of contacting grains may vary from $2l$ to $2L$. A sharp increase of $\mathcal{N}$ around $r=2R_v$ is still noticeable for oblate and prolate spheroids with $L/l=2$, but vanishes for extreme aspect ratios ($L/l=5$). The number $\mathcal{N}$ has been normalized by the solid volume fraction ϕ in Fig. 11(b). It is compared to its asymptotical long-range value

$$\mathcal{N}/\phi=(r/R_v)^3. \tag{16}$$

For aspherical particles, the departure from this regime vanishes very rapidly, and becomes negligible for $r\geqslant 3R_v$.

A complete exposition and discussion of these data for all shapes can be found in [23].

IV. TRANSPORT PROPERTIES OF RANDOM PACKINGS

A. Governing equations and methods of solution

In this section, the macroscopic effective coefficients for the basic transport processes by conduction, convection, and dispersion in random packed beds are determined. The governing equations and their methods of solution are briefly

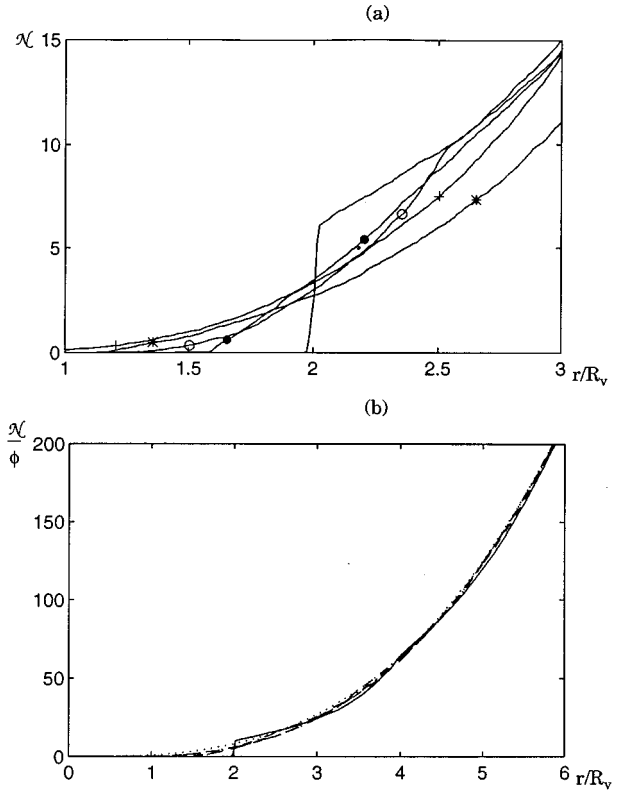

FIG. 11. The number $\mathcal{N}$ of particles within a distance r of a reference particle in random beds of aspherical ellipsoids as a function of the reduced distance r/R_v. Data in (a) are for $l_1/l_2=0.2$ (+), 0.5 (○), 1 (—), 2 (●), and 5 (∗). In (b), $\mathcal{N}$ is divided by ϕ and the dotted line is the asymptotic law (16).

recalled in this paragraph. They were detailed in earlier papers [40–42]. In all cases, the macroscopic coefficients are deduced by integrating the local fields, obtained by solving the transport equations at the pore scale.

Since the packings are macroscopically homogeneous, they are considered as infinite periodic media, made of identical unit cells. Note that the packings are indeed built with periodic conditions along the two horizontal directions. However, when a cubic sample is cut from a deposited bed, the lower and upper faces do not match each other. This may affect the computation of the transport properties along the vertical axis. The content of a unit cell is discretized into N_c^3 elementary cubes of size a. The unit cell size is $N_c a = w$. Whenever the center of an elementary cube falls in the solid (fluid) phase, the whole cube is considered as filled with solid (fluid). The following parameters were used in the computations; for series 1 and 2, $N_c=64$ and $4 \leqslant R_v/a \leqslant 8$; for series 3, $N_c=48$ and $R_v/a=3$ for calculating the dispersivity and the permeability and $N_c=64 R_v/a=4$ for the conductivity.

1. Conduction

The thermal terminology is used here, but the following developments are also valid for electrical conduction and for diffusion of Brownian particles whose size is small with respect to a typical size of the medium. Electrical and thermal conductions are both governed by a Laplace equation

$$\nabla^2 T = 0, \tag{17}$$

where T is the local field, together with the no-flux boundary condition at the wall S_p, when the solid phase is assumed to be insulating

$$\hat{\mathbf{m}} \cdot \boldsymbol{\nabla} T = 0 \quad \text{on } S_p, \tag{18}$$

where $\hat{\mathbf{m}}$ is the unit vector normal to S_p.

$\boldsymbol{\nabla} T$ is assumed to be spatially periodic with a period aN_c in the three directions of space. In addition, either the macroscopic temperature gradient $\overline{\boldsymbol{\nabla} T}$ or the average heat flux $\overline{\mathbf{q}}$,

$$\overline{\mathbf{q}} = \frac{1}{(aN_c)^3} \int_s \mathbf{q}\mathbf{R} \cdot ds, \tag{19}$$

is specified. S is the surface of the unit cell.

These two quantities are related by the symmetric positive definite conductivity tensor $\boldsymbol{\sigma}$:

$$\overline{\mathbf{q}} = -\sigma \cdot \overline{\boldsymbol{\nabla} T}, \tag{20}$$

which depends only upon the geometry of the medium.

In the average, for an isotropic random medium, σ is a spherical tensor equal to $\overline{\sigma}\,\mathbf{I}$. For deposited packings, the x and y directions play equivalent roles, but one may expect a different behavior along the z axis. In the following, $\overline{\sigma_{xy}}$ denotes the average of the conductivities along the x and y axes, which were indeed always found equal within the statistical fluctuations, and $\overline{\sigma_z}$ denotes the conductivity in the vertical direction.

The Neumann problem [Eqs. (17)–(19)] is solved via a second-order finite-difference formulation. A conjugate-gradient method turned out to be very effective for the problem at hand, primarily because it is better suited to vectorial programming than implicit relaxation schemes.

2. Stokes flow

The low Reynolds number flow of an incompressible Newtonian fluid is governed by the usual Stokes equations,

$$\begin{aligned} \boldsymbol{\nabla} p &= \mu \nabla^2 \mathbf{v}, \\ \boldsymbol{\nabla} \cdot \mathbf{v} &= 0, \end{aligned} \tag{21}$$

where $\mathbf{v}$, p, and μ are the velocity, pressure, and viscosity of the fluid, respectively. In general, $\mathbf{v}$ satisfies the no-slip condition at the wall

$$\mathbf{v} = \mathbf{0} \quad \text{on } S, \tag{22a}$$

where S denotes the surface of the wetted solid inside the unit cell. The volume τ_0 of this cell is equal to $(N_c a)^3$. Because of the spatial periodicity of the medium, it can be shown (see [43]) that $\mathbf{v}$ possesses the following property:

$$\begin{gathered} \mathbf{v} \text{ is spatially periodic,} \\ \text{with period } aNc \text{ in the three directions of space.} \end{gathered} \tag{22b}$$

This system of equations and conditions applies locally at each point $\mathbf{R}$ of the interstitial fluid. In addition, it is assumed that either the seepage velocity vector $\overline{\mathbf{v}}$ is specified, i.e.,

$$\overline{\mathbf{v}}=\frac{1}{\tau_0}\int_{\partial\tau_0}\mathbf{R}\mathbf{v}\cdot\mathbf{ds}=(\text{a prescribed constant vector}) \tag{23a}$$

or else the macroscopic pressure gradient $\overline{\nabla p}$ is specified,

$$\nabla p=(\text{a prescribed constant vector}). \tag{23b}$$

Since the system (21)–(23) is linear, it can be shown that $\overline{\mathbf{v}}$ is a linear function of $\overline{\nabla p}$. These two quantities are related by the permeability tensor $\mathbf{K}$ such that

$$\overline{\mathbf{v}}=-\left(\frac{1}{\mu}\right)\mathbf{K}\cdot\overline{\nabla p}. \tag{24}$$

Here $\mathbf{K}$ is a symmetric tensor that is positive definite. It only depends on the geometry of the system and thus can be simplified when the porous medium possesses geometric symmetries. As before, we denote by K_{xy} the average of the permeabilities along the x and y directions and by K_z the permeability along the z direction.

The numerical method that is used here is a fourth order finite difference scheme identical to the one first described by Lemaître and Adler [41] and later improved by Coelho [23]. In order to cope with the continuity equation, the so-called artificial compressibility method was applied with a staggered marker-and-cell (MAC) mesh [44].

3. Dispersion of a passive solute

The physical situation can be summarized as follows; a neutrally buoyant, spherical Brownian particle is injected at some arbitrary interstitial position $\mathbf{R}'$ at time $t=0$; this particle is convected by the interstitial fluid and simultaneously undergoes Brownian motion characterized by the diffusion coefficient D. Within the limit of long times, the moments of order m of the probability distribution are defined by [45]

$$\mathbf{M}_m=\int_{v_\infty}(\mathbf{R}-\mathbf{R}')^m P(\mathbf{R},t/\mathbf{R}')d^3\mathbf{R}, \tag{25}$$

where $(\mathbf{R}-\mathbf{R}')^m$ represents the m-adic $(\mathbf{R}-\mathbf{R}')\cdots(\mathbf{R}-\mathbf{R}')$. The probability density is denoted by $P(\mathbf{R},t/\mathbf{R}')$. The two first moments verify [45]

$$\lim_{t\to\infty}\frac{d\mathbf{M}_1}{dt}=\overline{\mathbf{v}}^*, \tag{26a}$$

$$\lim_{t\to\infty}\frac{1}{2}\frac{d}{dt}(\mathbf{M}_2-\mathbf{M}_1\mathbf{M}_1)=\overline{\mathbf{D}}^*, \tag{26b}$$

where $\mathbf{v}^*$ is the mean interstitial fluid velocity vector in τ_L, the portion of the unit cell τ_0 occupied by the liquid phase,

$$\overline{\mathbf{v}}^*=\frac{1}{\tau_L}\int_{\tau_L}\mathbf{v}\,d^3\mathbf{R}. \tag{27}$$

The general expression of the macroscopic dispersion tensor $\mathbf{D}^*$ is given by [45]

$$\overline{\mathbf{D}}^*=\frac{D}{\tau_L}\int_{\tau_L}\nabla\mathbf{B}^t\cdot\nabla\mathbf{B}d^3\mathbf{R}, \tag{28}$$

where $\mathbf{B}$ is a vector field satisfying

$$\mathbf{B}(\mathbf{R})=\check{\mathbf{B}}(\mathbf{R})-\mathbf{R} \tag{29}$$

where $\check{\mathbf{B}}$ is the spatially periodic component of $\mathbf{B}$ and is the solution of

$$\mathbf{v}-\overline{\mathbf{v}}^*=\nabla\cdot(\mathbf{v}\check{\mathbf{B}})-D\nabla^2\check{\mathbf{B}} \tag{30a}$$

$$\mathbf{n}\cdot\nabla\check{\mathbf{B}}=\mathbf{n}\quad\text{on } S_p. \tag{30b}$$

The flow field was first determined by the routine that yields permeability. The $\mathbf{B}$ equation was discretized by a second-order finite difference formulation and solved by a conjugate-gradient iterative scheme [42].

Because the flow provides a preferred direction, the dispersion tensor $\mathbf{D}^*$ in an isotropic medium can generally be written as

$$\overline{\mathbf{D}}^*=\begin{pmatrix}\overline{D_\parallel^*} & 0 & 0\\ 0 & \overline{D_\perp^*} & 0\\ 0 & 0 & \overline{D_\perp^*}\end{pmatrix}. \tag{31}$$

The x axis is assumed to be parallel to the interstitial velocity $\overline{\mathbf{v}}^*$, so that the y and z axes play an equivalent role. The situation is more complex in aspherical packings, and a full matrix is generally expected instead of Eq. (31). Owing to the disturbance induced by the mismatch of the upper and lower faces of the unit cell, vertical dispersion was never considered. The flow was set successively along the x and y axes, and the corresponding longitudinal and transverse (in the horizontal plane) dispersion coefficients were calculated. Their averages are denoted by $\overline{D_\parallel^*}$ and $\overline{D_\perp^*}$, respectively.

B. Conductivity

The conductivities of all the packed beds are plotted against the aspect ratio l_1/l_2 in Fig. 12. Sample results for series 3 are also given in Table II. The curves for $\overline{\sigma_{xy}}$ are very similar to the porosity curves in the same packings in Fig. 5. For unit aspect ratios, $\overline{\sigma_{xy}}$ is close to 0.2 for beds of spheres and cylinders, and to 0.24 for beds of cubes, which have a larger porosity. Our results for sphere packings are slightly lower than the experimental value of 0.25 reported by Pfannkuch [46] and Wong *et al.* [47] for random packings with porosities 0.39 and 0.40, respectively. For prolate particles, the conductivity increases with l_1/l_2 up to about 0.5 for $l_1/l_2=10$. For oblate cylinders and parallelepipeds, $\overline{\sigma_{xy}}$ increases also when the particles become flatter. For oblate ellipsoids, the conductivity increases only slightly, as does the porosity.

The vertical conductivity $\overline{\sigma_z}$ behaves differently. For prolate particles, it is identical to $\overline{\sigma_{xy}}$, since the packings are roughly isotropic, as shown by the weak orientational ordering (Figs. 8 and 9) and by the correlations R_{xy} and R_z (Fig. 10). However, for oblate cylinders and parallelepipeds, $\overline{\sigma_z}$ remains almost constant when l_1/l_2 decreases, although the porosity increases. This results from the layered structure of the beds, indicated by the parameters Q and M. For oblate ellipsoids, the porosity does not increase and Q tends toward one. Consequently, $\overline{\sigma_z}$ decreases significantly, down to 0.02 at $l_1/l_2=0.1$.

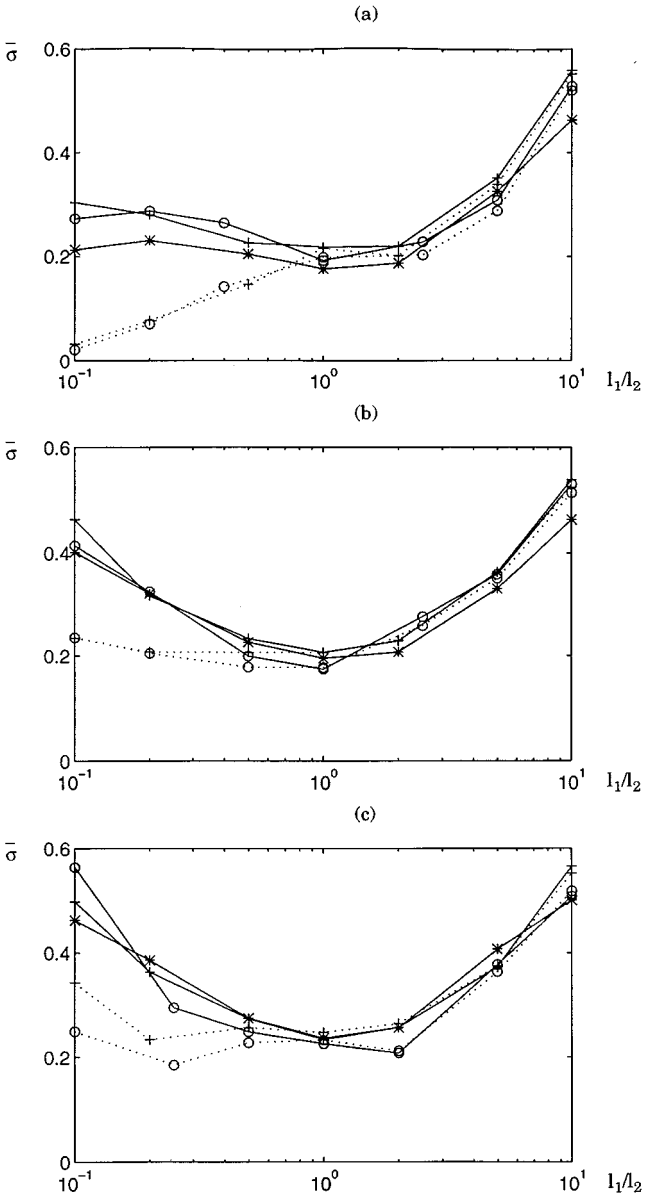

FIG. 12. The conductivities $\overline{\sigma_{xy}}$ (solid lines) and $\overline{\sigma_z}$ (dotted lines) of packed beds of ellipsoids (a), cylinders (b), and parallelepipeds (c) vs the aspect ratio l_1/l_2. Data are for series 1 (○), 2 (+), and 3 (∗).

The same data for $\overline{\sigma_{xy}}$ are recast in Fig. 13 against the bed porosity ϵ. It is remarkable that all the conductivity values, whatever the particle shape and elongation and for all the series (i.e., for a weighting length $\hat{R}$ from $0.1L$ to $2L$), are fairly well gathered around a single curve. The only exception is the small cloud of points above the curve at $\epsilon \approx 0.4$, which corresponds to beds of flat ellipsoids, i.e., to highly ordered packings.

The dependence of $\overline{\sigma_{xy}}$ upon porosity verifies the widely used Archie's Law [48]

$$\overline{\sigma} = \alpha \epsilon^m, \tag{32}$$

where the exponent m is the so-called cementation factor. It has been measured by several authors on different types of material, although always in a porosity range lower than ours. Jacquin [49] obtained $m=1.64$, $\alpha=0.80$ for Fontainebleau sandstones in the range $0.05 \leqslant \epsilon \leqslant 0.30$. Guillot [50] also observed a power law for sintered glass beads, with $m \approx 1.6$ for $0.1 \leqslant \epsilon \leqslant 0.40$. Her results are somewhat scattered because of sample heterogeneities; her most homogeneous samples yield $m \approx 1.4$. Wong *et al.* [47], using their own data and those of Johnson *et al.* [51] for fused-glass beads, obtained $m \approx 2.3$, $\alpha \approx 3.3$ for $0.02 \leqslant \epsilon \leqslant 0.2$ and $m \approx 1.5$, $\alpha \approx 1$ for $0.2 \leqslant \epsilon \leqslant 0.4$. Schwartz *et al.* [52] also obtained $m \approx 1.5$ for $\epsilon \geqslant 0.3$. Of course, the porosity variations in these media result generally from various degrees of consolidation by cementation (for sandstones) or by sintering (for beads). Therefore, results for low porosities cannot be directly extrapolated to looser unconsolidated packings.

If packings of prolate particles were built with very large aspect ratios, the porosity would tend toward unity, as well as $\overline{\sigma}$. Thus, if a unique expression of the form (32) is used to cover the whole range of porosity, the coefficient α has to be 1. A least square fit of the results excluding the ordered packings of oblate ellipsoids yields (cf. Fig. 13)

$$\overline{\sigma_{xy}} = \epsilon^{1.915}. \tag{33a}$$

Alternatively, the data can be fitted with a correlation coefficient $r=0.975$ as

$$\overline{\sigma_{xy}} = 0.880 \epsilon^{1.72}. \tag{33b}$$

The data of Kim *et al.* [33] for beds of mica particles and mylar disks are also plotted in Fig. 13. The agreement with our calculations is very good for the mica particles. Mylar disks yield slightly larger conductivities. Ochoa-Tapia *et al.* [53] noted that a cell model is able to predict $\overline{\sigma_z}$, but overestimates $\overline{\sigma_{xy}}$.

C. Permeability

The permeabilities for all the packed beds, normalized by R_v^2, are plotted in Fig. 14 versus the aspect ratio l_1/l_2. Sample results for series 3 are also given in Table II. These data can be commented upon in the same way as those for conductivity in Fig. 12. For unit aspect ratios, the permeability K_{xy} for spheres and cylinders is found in the range $2\times10^{-3}R_v^2 \leqslant K_{xy} \leqslant 3\times10^{-3}R_v^2$. Packings of cubes, with a slightly higher porosity, yield $3.5\times10^{-3}R_v^2 \leqslant K_{xy} \leqslant 4.5\times10^{-3}R_v^2$. The vertical permeability K_z is found equal to K_{xy} for $l_1/l_2=1$, as observed for conductivity. Our results for spheres are consistent with many experimental data. Chauveteau and Zaitoun [31] measured $2.3\times10^{-3} \leqslant K/r^2 \leqslant 4.1\times10^{-3}$ and $3.3\times10^{-3} \leqslant K/r^2 \leqslant 4.7\times10^{-3}$ for various glass bead packings with porosities 0.40 and 0.41, respectively. Pfannkuch [45] obtained $K/r^2=1.1\times10^{-3}$ and 2.3×10^{-3} for two bead packings with the same porosity 0.388. Guillot's [50] measurements for bead packings in the porosity range $0.39 \leqslant \epsilon \leqslant 0.41$ yielded $3.2\times10^{-3} \leqslant K/r^2 \leqslant 6.7\times10^{-3}$. Finally, Bryant *et al.* [28] calculated $K/r^2=2.72\times10^{-3}$ by use of a network model based on the geometrical data of Finney [54] for a monodisperse sphere packing.

For nonunit aspect ratios, K_{xy} increases as did $\overline{\sigma_{xy}}$ in Fig. 12, i.e., according to the porosity variations. In particular, permeabilities for oblate ellipsoid packings do not differ much from that of sphere packings.

TABLE II. Samples results for packings of series 3. The sample size w/L, the porosity ϵ, the orientational parameters M and Q, the number of grains in the sample N_u, the conductivity $\overline{\sigma_{xy}}$, and the permeability K_{xy}/R_v^2 are given for various aspect ratios l_1/l_2.

l_1/l_2	w/L	ϵ	M	Q	N_u	$\overline{\sigma_{xy}}$	$10^3 K_{xy}/R_v^2$
				Ellipsoids			
0.1	7.43	0.395	0.986	0.993	592	0.212	1.59
0.2	9.36	0.428	0.880	0.938	559	0.230	2.29
0.5	12.70	0.412	0.702	0.838	575	0.205	2.02
1.0	12.50	0.403	0.072	0.261	279	0.177	2.16
2.0	10.08	0.415	0.116	0.682	572	0.188	1.77
5.0	5.47	0.567	0.143	0.748	423	0.325	7.39
10.0	3.45	0.688	0.097	0.628	305	0.464	19.62
				Cylinders			
0.1	8.50	0.669	0.365	0.605	324	0.402	16.65
0.2	10.71	0.540	0.506	0.712	450	0.321	8.17
0.5	14.54	0.472	0.086	0.290	516	0.226	3.39
1.0	18.32	0.448	0.002	0.063	540	0.196	2.58
2.0	11.54	0.459	0.008	0.192	529	0.208	2.63
5.0	6.26	0.580	0.089	0.582	411	0.331	8.36
10.0	3.95	0.693	0.024	0.323	300	0.464	20.25
				Parallelepipeds			
0.1	9.21	0.714	0.358	0.598	280	0.462	22.06
0.2	11.61	0.628	0.276	0.526	364	0.386	14.23
0.5	14.53	0.531	0.072	0.271	459	0.275	5.76
1.0	19.85	0.497	0.012	0.103	492	0.237	4.33
2.0	12.51	0.519	0.005	0.088	470	0.257	4.76
5.0	6.23	0.647	0.035	0.374	345	0.407	15.61
10.0	4.28	0.719	0.056	0.476	275	0.500	25.47

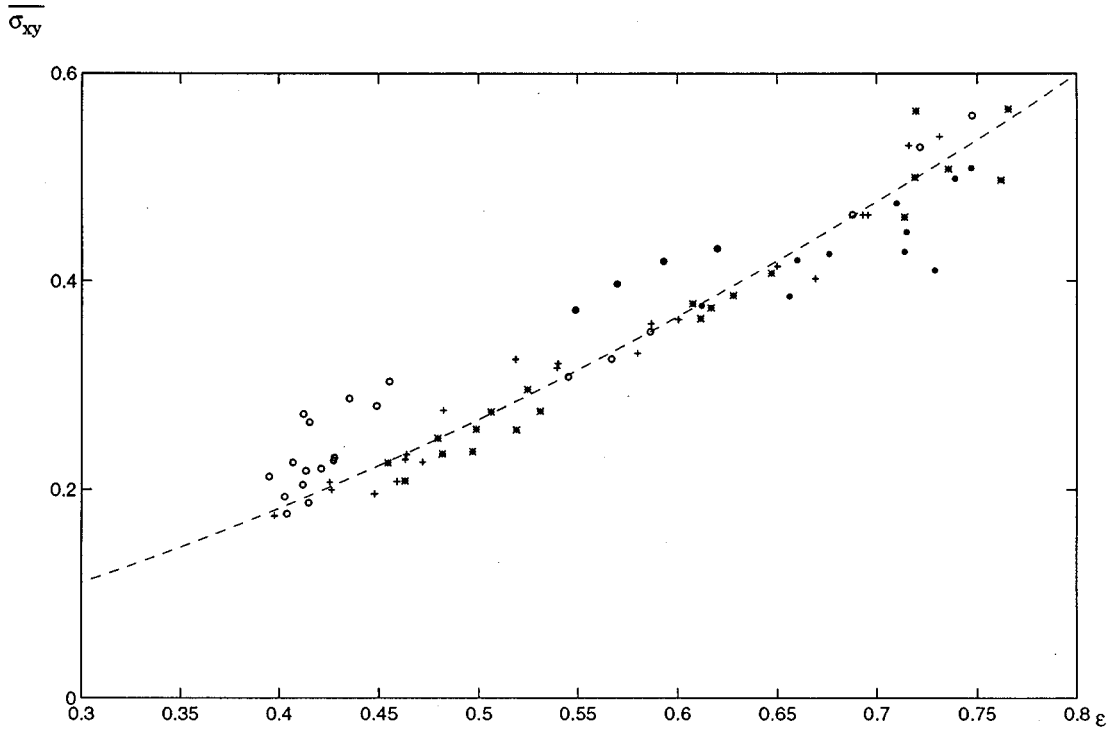

FIG. 13. The conductivity $\overline{\sigma_{xy}}$ of random beds of ellipsoids (○), cylinders (+), and parallelepipeds (∗) vs the porosity ϵ. The broken line is (33). (●) and (⊕) are Kim *et al.* [33] data for beds of mica particles and of mylar disks, respectively.

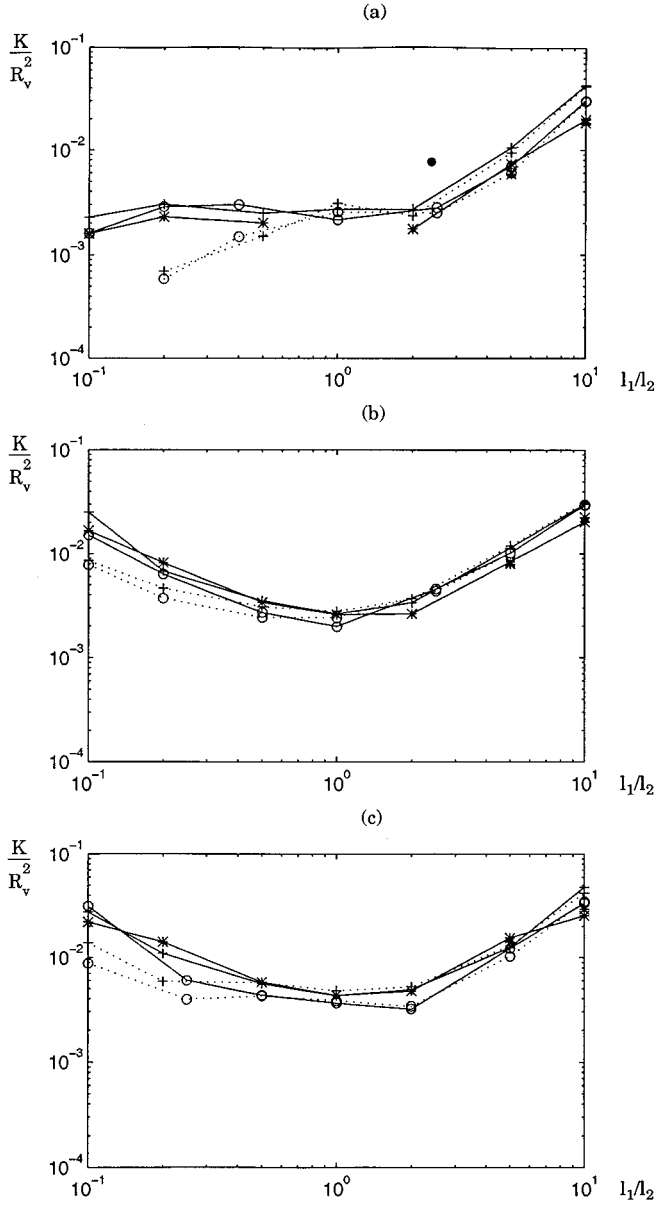

FIG. 14. The permeabilities K_{xy}/R_v^2 (solid lines) and K_z/R_v^2 (dotted lines) of beds of ellipsoids (a), cylinders (b), and parallelepipeds (c) vs the aspect ratio l_1/l_2. Data are for series 1 (○), 2 (+), and 3 (∗). The dot (●) is the measurement of Thiess-Weesie *et al.* [34].

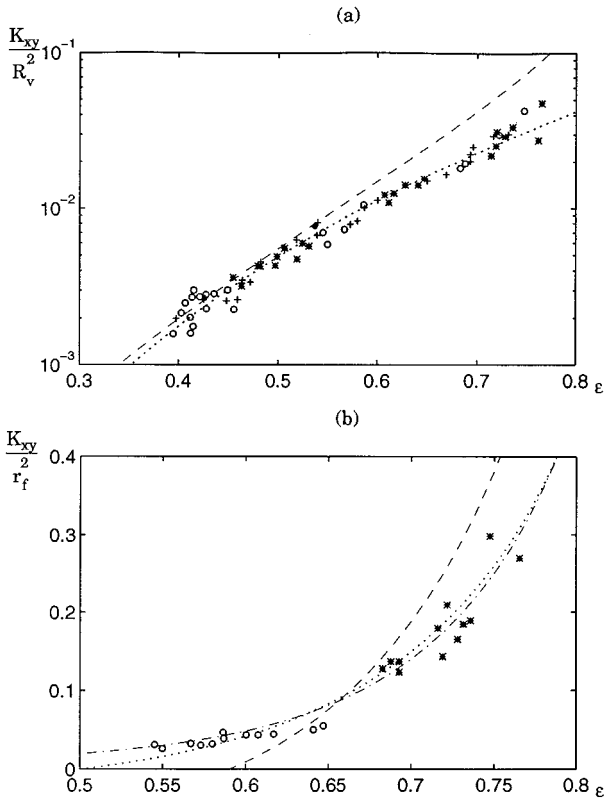

FIG. 15. Permeability as function of porosity. (a) K_{xy}/R_v^2 of random beds of ellipsoids (○), cylinders (+), and parallelepipeds (∗) vs the porosity ϵ. The dot is the measurement of Thiess-Weesie *et al.* [34]. The broken line is Eq. (34c) with $k/\Psi^2=10$; the dotted line is the least square fit Eq. (41). (b) The permeability K_{xy}/r_f^2 of random beds of prolate particles with $L/l=5$ (○) and 10 (∗) vs the porosity ϵ. The broken line is Eq. (37) with $k_4=6.1$ and $k_5=0.64$. The dotted line is Eq. (37) with $k_4=12.6$ and $k_5=0.707$. The dashed line is Eq. (38).

The vertical permeability K_z also behaves in a way similar to the vertical conductivity σ_z. For prolate particles, K_{xy} and K_z are roughly identical since the packed beds are isotropic. For oblate grains, K_z is lower than K_{xy}, especially for flat ellipsoids, which yield the most ordered stratified structures.

The data in Fig. 14 for K_{xy} are recast in Fig. 15(a) as functions of the bed porosity ϵ. Again, it is remarkable that the simple normalization of K_{xy} by the square equivalent radius R_v^2 gathers the results for the various shapes and elongations around a single master curve. The mode of construction of the packings, with the weighting length $\hat{R}$ in Eq. (2b), does not seem to have any influence when beds with identical porosities are compared.

The permeability of packed beds, or more generally of porous media, has been extensively studied in the literature, although in a range of porosities lower than the present one. Several empirical or semiempirical models have been proposed to rationalize its dependence upon global parameters such as porosity, the hydraulic radius, or the specific surface area (cf., for example, [55] or [56]). The most classical model is the Carman-Kozeny equation [57]

$$K=\frac{\epsilon m^2}{k}, \tag{34a}$$

where k is the so-called Kozeny constant. k is generally a few units. For sphere packings, the value $k=5$ is widely accepted. With the definition Eqs. (7) and (34a) can be recast into

$$\frac{K}{R_v^2}=\frac{\epsilon^3}{k\mathcal{S}^2}. \tag{34b}$$

Since for well defined particle shapes the specific surface area is directly related to the porosity by Eqs. (6) and (34b) for grain packings may be written as

$$\frac{K}{R_v^2}=\frac{\epsilon^3\Psi^2}{9k(1-\epsilon)^2}. \tag{34c}$$

Martys *et al.* [20] could accurately represent the results of numerical calculations for nine different models of porous media, including seven types of random sphere packings in the range $0.3\leqslant\epsilon\leqslant0.8$ by Eq. (34a) with $k=2$. However, none of these packings results from a grain deposition process, with mechanical stability requirements. The looser ones are actually suspensions, and in most cases the grains are allowed to overlap. These authors proposed also a universal scaling law for the porosity-permeability relation, valid in a very wide porosity range $0.02\leqslant\epsilon<1$. However, this law assumes the existence of a percolation threshold, which can exist only if the particles may overlap.

If the Carman-Kozeny model Eq. (34c) applies to the present packed beds, the unique master curve in Fig. 15(a) suggests that the Kozeny constant for aspherical grains is related to their asphericity index Ψ. Namely, if k_0 corresponds to spherical particles ($\Psi=1$), one should have for other shapes

$$k=\Psi^2k_0. \tag{35}$$

Equation (34c) is plotted in Fig. 15(a) with $k_0=10$, to fit our data for sphere packings. This value is much larger than the standard $k_0=5$, but recall that the actual surface area in the discretized samples is not equal to the theoretical value (6). On one hand, the grain contacts are nonpointwise, which lowers the specific area; on the other hand, the discretization of the grain surfaces has the opposite effect. As a whole, the discrete estimate of $\mathcal{S}$ overpredicts it by a factor of 1.2 to 1.4 in almost all cases, except for very oblate particles where this factor is very scattered. Thus, the use of $k_0=10$ in Eq. (34c) actually corresponds to $k\approx6$ in Eq. (34b) with the discrete estimate of $\mathcal{S}$. As seen in Fig. 15(a), the Carman-Kozeny model applies fairly well to these random packings for porosities up to 0.55. For looser beds, the model overestimates the permeability.

The discrepancy at high porosities may result from the heuristic argument underlying the Carman-Kozeny equation. The pore space is viewed as a network of capillaries or plane channels, and this becomes unrealistic for loose beds. In particular, packings of very prolate particles are closer to fibrous beds, which have given rise to other types of empirical correlations (cf. the review in [25]). The permeability is generally normalized by an equivalent fiber radius r_f:

$$r_r=\left(\frac{\phi}{\pi L}\right)^{1/2}, \tag{36a}$$

where L is the total fiber length per unit volume. With our notations,

$$r_f=\left(\frac{2}{3}\frac{R_v}{L}\right)^{1/2}R_v. \tag{36b}$$

For isotropic fibrous beds, Chen [58] proposed the model

$$K/r_f^2=\frac{\pi(1-\phi)}{k_4\phi}\ln[k_5\phi^{-1/2}]. \tag{37}$$

He could fit a variety of experimental data with $k_4=6.1$ and $k_5=0.64$. This relation is compared to our results for slender particles with $L/l=5$ and 10 in Fig. 15(b). The agreement is not good if the previous constants are used, but is significantly improved if one sets $k_4=12.6$ and $k_5=0.707$. The major drawback of this model is that it predicts a percolation threshold at $\phi=k_5^2$, which limits its validity to very high porosities. Another empirical model due to Davies [59] is very successful:

$$K/r_f^2=[16\phi^{1.5}(1+64\phi^3)]^{-1}. \tag{38}$$

Very good agreement is observed in Fig. 15(b) for all prolate grain packings with $L/l\geqslant5$, without adjusting the constants in Eq. (38).

Another type of porosity-permeability correlation is commonly used, which does not involve the hydraulic radius, namely, the power law

$$K\alpha\epsilon^n. \tag{39}$$

Jacquin's [49] measurements on various Fontainebleau sandstones yielded $n\approx4.15$ in a porosity range $0.1\leqslant\epsilon\leqslant0.25$. Guillot [50] obtained the same value $n\approx4.16$ for fused glass beads with $0.2\leqslant\epsilon\leqslant0.44$. Rumpf and Gumpte [60] correlated numerous permeability measurements for polydisperse sphere packings by the power law

$$\frac{K}{\widetilde{D}^2}=\frac{\epsilon^{5.5}}{5.6}, \tag{40}$$

where $\widetilde{D}$ is a surface-weighted average grain diameter. As shown by Fig. 15(a), our data agree with Jacquin's [49] and Guillot's [50] results. A least square fit yields

$$\frac{K}{R_v^2}=0.117\epsilon^{4.57}\quad(r=0.988). \tag{41}$$

Finally, it has often been attempted to relate the conductivity and permeability of porous media. The conductivity and permeability measurements of Wong *et al.* [47] in fused glass bead packings with $0.02\leqslant\epsilon\leqslant0.4$ obey the scaling law

$$K\alpha\overline{\sigma^2}. \tag{42a}$$

Schwartz *et al.* [61] obtained the same dependence from the results of numerical simulations on various types of random packings whose porosity was varied from 0.1 to 0.55 by varying the grain radii and allowing overlaps. Katz and Thompson [62] obtained quantitative predictions for rocks with the model

$$K=cl_c^2\overline{\sigma}, \tag{42b}$$

where l_c is a characteristic length for the restrictions in the pore space controlling the flow, measured, for example, by mercury porosimetry. Even if the data in Fig. 16(a) corresponding to the ordered packings of oblate ellipsoids are omitted, our results do not fall between Eqs. (42a) and (42b). A least squares fit yields

$$K=0.158\overline{\sigma}^{2.53}\quad(r=0.984), \tag{43}$$

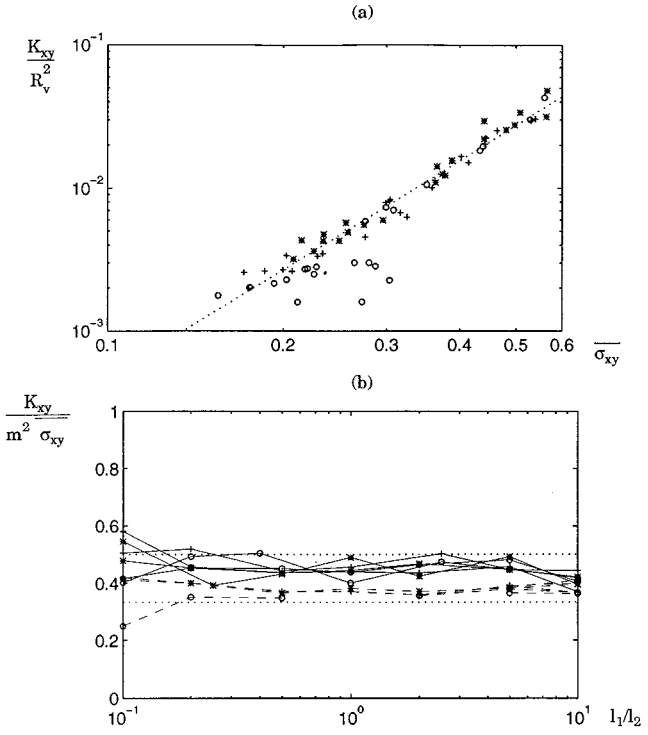

FIG. 16. Relation between permeability and conductivity. (a) The permeability K_{xy}/R_v^2 of beds of ellipsoids (○), cylinders (+), and parallelepipeds (∗) vs the conductivity $\overline{\sigma_{xy}}$. The dotted line is Eq. (43). (b) The ratio $K_{xy}/m^2\overline{\sigma_{xy}}$ for packings of ellipsoids (○), cylinders (+), and parallelepipeds (∗) vs the aspect ratio l_1/l_2. Data are for series 1 and 2 (—) and series 3 (---).

in a good agreement with the combination of Eqs. (33b) and (41).

An interesting model was proposed by Berryman and Blair [63], following Walsh and Brace [64]. If the pore space is viewed as a plane or circular channel, it may be shown that

$$K=\frac{m^2}{b}\,\overline{\sigma},\tag{44a}$$

where b is 2 for tubes and 3 for cracks. For well defined grain shapes, Eq. (44a) may be recast into

$$\frac{K}{R_v^2}=\frac{\epsilon^2\Psi^2}{9(1-\epsilon)^2 b}\,\overline{\sigma}.\tag{44b}$$

The ratio $K_{xy}/m^2\overline{\sigma_{xy}}$ is plotted in Fig. 16(b) as a function of the aspect ratio l_1/l_2 for all the packed beds considered in this paper with m evaluated on the discretized geometries. Except for $l_1/l_2=0.1$, where the data are more scattered, it is always found between 1/3 and 1/2, corresponding to the two values of b mentioned above.

Let us finally compare our results to the few data relative to aspherical grain packings in the literature. In their packed beds of prolate ellipsoids obtained by filtration (see Sec. III A), Thiess-Weesie *et al.* [34] measured $K/R_v^2=7.7\times10^{-3}$ for $l_1/l_2=2.37$, $\epsilon=0.54$. Since their porosity is higher than ours for identical particle elongations [cf. Fig. 5(a)] this result does not fall with our data in the plot of K/R_v^2 versus l_1/l_2 in Fig. 14. However, it agrees very well with the permeabilities obtained for beds with the same porosity [Fig. 15(a)]. This illustrates again the fact that the deposited packing transport properties do not depend upon their mode of construction, provided that it does not induce any grain ordering, when beds with identical porosities and equivalent particle size R_v are compared.

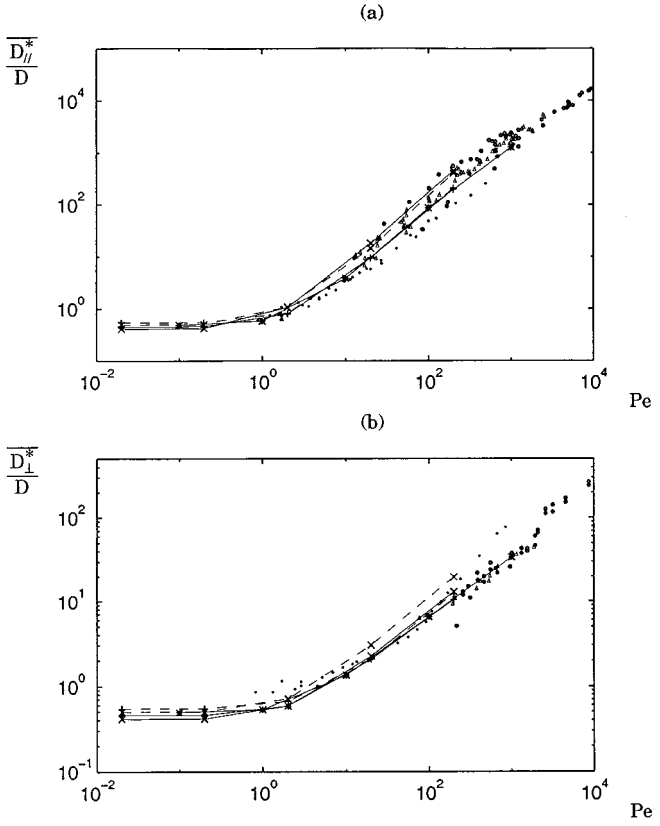

FIG. 17. The reduced axial $\overline{D_{\parallel}^*}/D$ (a) and transversal $\overline{D_{\perp}^*}/D$ (b) dispersion coefficients vs the Péclet number Pe. Numerical simulations for spheres (solid line with ∗) and ellipsoids with $l_1/l_2=0.5$ (short dashed line with +), 2 (long dashed line with +), 0.2 (dashed line with ×), and 5 (solid line with ×). Experimental data for bead packings: [66] (●); in (a) [45] for sands (△), and bead packings (○); in (b) [68] (△) and [67] (○) for bead packings.

D. Taylor dispersion

Since it is computationally much more demanding, dispersion has not been investigated as thoroughly as conductivity and permeability. Beds of ellipsoids were considered, with aspect ratios $l_1/l_2=0.2$, 0.5, 1, 2, and 5. The corresponding porosities were 0.401, 0.425, 0.409, 0.418, and 0.536. The sample size was $w/L=20/3$, except for spheres, with $w/L=15/2$. As mentioned in Sec. IV A, the flow direction was set along the x and y axes. The two axial and transverse (in the horizontal plane) dispersivity coefficients were found identical within a few percents. Their averages are denoted $\overline{D_{\parallel}^*}$ and $\overline{D_{\perp}^*}$, respectively.

The results are plotted in Fig. 17(a), versus the Péclet number Pe (see also Table III)

$$\mathrm{Pe}=\frac{v^* R_v}{D},\tag{45}$$

TABLE III. Axial and transverse dispersion coefficients in beds of ellipsoids with various aspect ratios l_1/l_2 as functions of the Péclet number Pe.

l_1/l_2	w/L	ϵ	Pe	$\overline{D_\parallel^*}$	$\overline{D_\perp^*}$
0.20	6.67	0.401	0.020	0.498	0.498
			0.20	0.506	0.502
			2.00	1.09	0.718
			20.0	14.8	3.05
			200	395	19.6
0.50	6.67	0.425	0.020	0.546	0.546
			0.200	0.550	0.550
			2.00	0.831	0.664
			20.0	9.54	2.12
			200	205	12.3
1.00	7.50	0.409	0.100	0.490	0.494
			1.00	0.588	0.534
			10.0	3.91	1.36
			100	85.5	6.51
			1000	1250	33.9
2.00	6.67	0.418	0.020	0.455	0.457
			0.20	0.460	0.457
			2.00	0.796	0.589
			20.0	9.74	2.08
			200	194	10.4
5.00	6.67	0.536	0.020	0.411	0.412
			0.20	0.422	0.415
			2.00	1.08	0.588
			20.0	18.4	2.27
			200	443	13

where D is the molecular diffusion coefficient and v^* is the mean interstitial fluid velocity, $v^*=\overline{v}/\epsilon$. The most striking feature is that, when cast against the Péclet number based on the equivalent radius R_v (45), the dispersion coefficients depend very little upon the particle shape, except in the diffusive regime Pe$\leqslant$1 where $\overline{D_\parallel^*}$ and $\overline{D_\perp^*}$ reduce to $\overline{\sigma_{xy}}/\epsilon$. The axial coefficients for spheres and oblate or prolate ellipsoids with $L/l=2$ are indistinguishable in the log-log plot of Fig. 17(a). The values of $\overline{D_\parallel^*}$ for very aspherical prolate and oblate grains with $L/l=5$ are almost identical, but the former differ by about a factor 2. The data for the transverse coefficients in Fig. 17(b) are even closer together. Only the very oblate ellipsoids with $l_1/l_2=0.2$ yield coefficients about 50% larger than the others. Note that the bed of slender ellipsoids with $l_1/l_2=5$, which has a much larger porosity (0.536 versus 0.4–0.425), does not show any peculiar behavior.

We are not aware of any systematic experimental study of dispersion in beds of very aspherical particles. However, measurements of axial dispersion in beds of spheres or of moderately irregular grains such as sands have given rise to numerous publications in the late 1950s. These were collected by Pfannkuch [46]. This collection was reproduced with little additions in later reviews [65,55,25,66]. Pfannkuch also performed measurements on sands and bead packings. Since they agree with the previous results, they are reproduced with the later results of Gunn and Pryce [67] and compared with our calculations in Fig. 17(a). From the photographs in Pfannkuch [46], the typical aspect ratio of his sand grains may be roughly estimated as $L/l=2$. His data for sands and bead packings are very similar, and lie mostly between our curves for $L/l=1$ or 2 and $L/l=5$. Gunn and Pryce [67] data are lower than our data for spheres by a factor less than 2.

Experimental data for transverse dispersion are fewer, but since they are more recent and have the benefit of improved measurement techniques, they are considered as valid and accurate as those obtained for longitudinal dispersion [65]. The data in Fig. 17(b) were obtained by Harleman and Rumer [68], Gunn and Pryce [67] and Han *et al.* [69] in sphere packings with porosities 0.36, 0.37, and 0.39–0.41, respectively. The agreement with our data for spheres is again very good.

It is common practice to relate the dispersion coefficient to the Péclet number by a power law:

$$\overline{D^*}\propto \mathrm{Pe}^n. \tag{46}$$

From the data in Fig. 17(a), the exponent n for the axial coefficient $\overline{D_\parallel^*}$, measured around Pe=100, is equal to 1.27 for spheres and moderately aspherical grains and to 1.40 for very aspherical ones. A lower exponent is obtained for $\overline{D_\perp^*}$ in Fig. 17(b); n is equal to 0.71 for spheres and moderate aspect ratios and to 0.78 for very aspherical particles. A least square fit of all the data for Pe$\geqslant$10 yields

$$D_\parallel^*/D=0.26\mathrm{Pe}^{1.29},\quad r=0.98,\quad \mathrm{Pe}\geqslant 10,$$

$$D_\perp^*/D=0.27\mathrm{Pe}^{0.72},\quad r=0.98,\quad \mathrm{Pe}\geqslant 10. \tag{47}$$

The exponents in Eq. (47) are consistent with the experimental determinations for various unconsolidated media. For axial dispersion the most common value is 1.2 [70,65]. For transverse dispersion, the exponent ranges from 0.67 [68] to 1.1 [65]. The ratio of $D_{\parallel}^{*}$ and $D_{\perp}^{*}$ is very close to the experimental observation of Harleman and Rumer [68]:

$$\overline{D_{\parallel}^{*}}/\overline{D_{\perp}^{*}} \propto \mathrm{Pe}^{1/2} \tag{48}$$

V. CONCLUSION

While the geometric properties of grain packings obviously depend on the geometry of the constituting grains, it has often been pointed out that they depend also upon the mode of construction. For example, the random sequential deposition algorithms in this work or in previous contributions yield much smaller porosities for identical particles than the Monte Carlo simulations of Buchalter and Bradley [14]. The experimental observations are also scattered, due to different packing procedures. Even within the framework of the present algorithm, the weighting length $\hat{R}$, which corresponds to specific operating conditions, has some impact on the bed structure.

Perhaps the most striking result in this paper is the fact that the effective transport properties of the packed beds are totally oblivious to these circumstances. Except for oblate ellipsoids, which yield highly ordered structures, all the beds with identical porosities share almost identical conductivities, permeabilities, and dispersion coefficients, regardless of grain shape or construction mode. This suggests the existence of a very general class of ''random unconsolidated granular media,'' whose transport coefficients depend only upon porosity and an equivalent grain size R_v. This would explain the good agreement that is always obtained between numerical simulations and experimental observations for all the transport processes. This would also explain the variety of situations where simple models like Archie's law or the Carman-Kozeny equation can be successfully applied. Our computations can be summarized by Eqs. (33), (41), and (47), which are verified with a correlation coefficient r larger than 0.975.

[1] J. G. Berryman, Phys. Rev. A **27**, 1053 (1983).
[2] R. M. German, *Particle Packing Characteristics* (Metal Powder Industry Federation, Princeton, 1989).
[3] J. L. Chermant (unpublished).
[4] P. Meakin and A. T. Skjeltrop, Adv. Phys. **42**, 1 (1993).
[5] G. C. Barker, in *Granular Matter—An Interdisciplinary Approach*, edited by A. Mehta (Springer-Verlag, Berlin, 1993).
[6] M. J. Vold, J. Phys. Chem. **64**, 1616 (1960).
[7] W. M. Visscher and M. Bolsterli, Nature **239**, 504 (1972).
[8] R. Jullien and P. Meakin, Europhys. Lett. **4**, 1385 (1987).
[9] R. Bacri *et al.*, Europhys. Lett. **2**, 123 (1986).
[10] G. Y. Onada and E. G. Liniger, Phys. Rev. Lett. **64**, 2727 (1990).
[11] A. Rosato, F. Prinz, K. J. Strandburg, and R. H. Swendsen, Powder Technol. **49**, 59 (1986).
[12] A. Rosato, K. J. Strandburg, F. Prinz, and R. H. Swendsen, Phys. Rev. Lett. **58**, 1038 (1987).
[13] B. J. Buchalter and R. M. Bradley, Phys. Rev. A **46**, 3046 (1992).
[14] B. J. Buchalter and R. M. Bradley, Europhys. Lett. **26**, 159 (1994).
[15] K. Z. Y. Yen and T. K. Chaki, J. Appl. Phys. **71**, 3164 (1992).
[16] C. H. Bennet, J. Appl. Phys. **43**, 2727 (1972).
[17] R. Jullien, P. Meakin, and A. Pavlovitch, Phys. Rev. Lett. **69**, 640 (1992).
[18] W. S. Jodrey and E. M. Tory, Phys. Rev. A **32**, 2347 (1985).
[19] R. E. Larson and J. J. L. Higdon, Phys. Fluids A **1**, 38 (1989).
[20] N. S. Martys, S. Torquato, and D. P. Bentz, Phys. Rev. E **50**, 403 (1994).
[21] S. Torquato and G. Stell, J. Chem. Phys. **82**, 980 (1985).
[22] J. A. Dodds, J. Colloid Interface Sci. **77**, 317 (1980).
[23] D. Coelho, Ph.D. thesis, Poitiers, 1996 (unpublished).
[24] G. Matheron, *Eléments pour une Théorie des Milieux Poreux* (Masson, Paris, 1967).
[25] F. A. L. Dullien, *Porous Media. Fluid Transport and Pore Structure* (Academic, New York, 1992).
[26] M. Dixmier, J. Phys. (Paris) **39**, 873 (1978).
[27] M. J. Kwiecien, I. F. MacDonald, and F. A. L. Dullien, J. Microsc. **159**, 343 (1990).
[28] S. L. Bryant, P. R. King, and D. W. Mellor, Trans. Porous Media **11**, 53 (1993).
[29] S. L. Bryant, G. Mason, and D. W. Mellor, J. Colloid Interface Sci. **177**, 88 (1996).
[30] J. F. Thovert, J. Sallès, and P. M. Adler, J. Microsc. **170**, 65 (1993).
[31] G. Chauveteau and A. Zaitoun, *European Symposium on Enhanced Oil Recovery Proceedings* (Elsevier Sequoia, Lauzanne, 1981), p. 197.
[32] A. P. Philipse and C. Pathmamanoharan, J. Colloid Interface Sci. **159**, 96 (1993).
[33] J. H. Kim, J. A. Ochoa, and S. Whitaker, Trans. Porous Media **2**, 327 (1987).
[34] D. M. E. Thies-Weesie, A. P. Philipse, and S. G. I. M. Kluijtmans, J. Colloid Interface Sci. **174**, 211 (1995).
[35] J. Warren and R. M. German, *Modern Developments in Powder Metallurgy*, Vol. 18, edited by P. M. Gummeson and D. A. Gustatson (Metal Powder Industries Federation, New Jersey, 1988), pp. 391–402.
[36] J. G. Berryman, J. Math. Phys. **28**, 244 (1987).
[37] G. K. Batchelor, Annu. Rev. Fluid Mech. **6**, 227 (1974).
[38] A. Acrivos and E. Chang, Phys. Fluids **29**, 3 (1986).
[39] S. Torquato, Rev. Chem. Eng. **4**, 151 (1987).
[40] J. F. Thovert, F. Wary, and P. M. Adler, J. Appl. Phys. **68**, 3872 (1990).
[41] R. Lemaître and P. M. Adler, Transp. Porous Media **5**, 325 (1990).
[42] J. Sallès, J. F. Thovert, R. Delannay, L. Prevors, J. L. Auriault, and P. M. Adler, Phys. Fluids A **5**, 2348 (1993).
[43] A. Benssoussan, J. L. Lions, and G. Papanicolaou, *Asymptotic Analysis for Periodic Structures* (North-Holland, Amsterdam, 1978).

[44] R. Peyret, T. D. Taylor, *Computational Methods for Fluid Flow*, Springer Series in Computational Physics (Springer-Verlag, Berlin, 1985).
[45] H. Brenner, Philos. Trans. R. Soc. London A **297**, 81 (1980).
[46] H. O. Pfannkuch, Rev. Inst. Fr. Pétrole, **18**, 215 (1963).
[47] P.-Z. Wong, J. Koplik, and J. P. Tomanic, Phys. Rev. B **30**, 6606 (1984).
[48] G. E. Archie, Trans. AIME **146**, 54 (1942).
[49] C. G. Jacquin, Revue IFP **19**, 921 (1964).
[50] D. Guillot, Thèse, ENSM, Paris, 1982 (unpublished).
[51] D. L. Johnson, T. J. Plona, C. Scala, F. Pasierb, and H. Kojima, Phys. Rev. Lett. **49**, 1840 (1982).
[52] L. M. Schwartz, J. R. Banavar, and B. I. Halperin, Phys. Rev. B **40**, 9155 (1989).
[53] J. A. Ochoa-Tapia, P. Stroeve, and S. Whitaker, Chem. Eng. Sci. **49**, 709 (1994).
[54] J. L. Finney, Proc. R. Soc. London A **319**, 479 (1970).
[55] J. Bear, *Dynamics of Fluids in Porous Media* (Dover, New York, 1988).
[56] P. M. Adler, *Porous Media. Geometry and Transport* (Butterworth-Heinemann, Stoneham, 1992).
[57] P. C. Carman, Trans. Inst. Chem. Engrs. (Lond.) **15**, 150 (1937).
[58] C. Y. Chen, Chem. Rev. **55**, 595 (1955).
[59] C. N. Davies, Proc. Inst. Mech. Eng. **1B**, 185 (1952).
[60] H. Rumpf and A. R. Gupte, Chem. Ing. Tech. **43**, 367 (1971).
[61] L. M. Schwartz, N. Martys, D. P. Bentz, E. J. Garboczi, and S. Torquato, Phys. Rev. E **48**, 4584 (1993).
[62] A. J. Katz and A. H. Thompson, Phys. Rev. B **34**, 8179 (1986).
[63] J. G. Berryman and S. C. Blair, J. Appl. Phys. **62**, 2221 (1987).
[64] J. B. B. Walsh and W. F. Brace, J. Geophys. Res. **89**, 9425 (1984).
[65] J. J. Fried and M. A. Combarnous, Adv. Hydroscience **7**, 169 (1971).
[66] M. Quintard and S. Whitaker, Chem. Eng. Sci. **48**, 2537 (1993).
[67] D. J. Gunn and C. Pryce, Trans. Inst. Chem. Eng. **47**, 341 (1969).
[68] D. R. F. Harleman and R. R. Rumer, J. Fluid Mech. **16**, 385 (1963).
[69] N. W. Han, J. Bhakta, and R. G. Carbonell, AICHE J. **31**, 277 (1985).
[70] G. A. Gist, A. H. Thompson, A. J. Katz, and R. L. Itiggins, Phys. Fluids A **2**, 1533 (1990).